On Chip Hybrid Photonic Crystal Surface Emitting Lasers

by

Shih-Chia Liu

Presented to the Faculty of the Graduate School of

The University of Texas at Arlington in Partial Fulfillment

of the Requirements

for the Degree of

DOCTOR OF PHILOSOPHY OF ELECTRICAL ENGINEERING

THE UNIVERSITY OF TEXAS AT ARLINGTON

December 2017

Acknowledgements

First and foremost, I would like to thank my supervisor Professor Weidong Zhou for his mentorship and guidance in the past five years. I appreciate all his contributions of time, ideas, and funding to make my Ph.D. experience productive and stimulating. The joy and enthusiasm he has for research was inspirational and motivational for me. It has been an honor to be his Ph.D. student.

I would also like to express my appreciations to my committee members, Professor Michael Vasilyev, Professor J.-C. Chiao, Professor Yuze (Alice) Sun, and Professor Ganesh Balakrishnan. Special thanks to Professor Ganesh Balakrishnan from University of New Mexico, for his time and attention. Thank to our collaborators Professor Zhenqiang (Jack) Ma at University of Wisconsin-Madison on nanomembrane transfer printing. Thank to our collaborators Professor Xiuling Li at University of Illinois Urbana-Champaign on materials growth. Thank to Professor Mattias Hammar from KTH Royal Institute of Technology in Stockholm for their work on QW material growth.

I would like to acknowledge honorary group member Dr. Hongjun, Dr. Deyin Zhao, and Dr. Laxmy Menon for their help, teaching and collaboration during my study in UTA. I would like to thanks my lab mates Dr. Xiaochen, Dr. Jin Huang, and Yonghao for their help, collaboration and helpful discussion. Thanks Zhonghe and Akhil for their help in and out of the cleanroom. I am grateful for the NANOFAB members Dr. Nader Hozhabri, Dennis, Kevin, and Mick for all their help on cleanroom tools. My thanks to UT Austin MRC facilities, staffs and my friends there for their kind helps and supports during the past four years.

Lastly, I would like to thank my family for all their love and encouragement. I am particularly grateful to my parents who raised me with a love of environment and

supported me in all my pursuits. Thanks to my sister and brother at Taiwan for their blessings and wishes. And most of all for my supportive, encouraging, and patient wife Weichu whose faithful support during the final stages of this Ph.D. is so appreciated. Thank you.

December 04, 2017

Abstract

On Chip Hybrid Photonic Crystal Surface Emitting Lasers

Shih-Chia Liu, PhD

The University of Texas at Arlington, 2017

Supervising Professor: Name WEIDONG ZHOU

Remarkable progresses have been made over the recent years on silicon photonics by utilizing the complementary metal-oxide-semiconductor (CMOS) compatible process, which is capable of producing devices and integrated IC chips at low cost and in mass volumes. CMOS compatible lasers on silicon (Si) remain an active and challenging area of research for integrated Si photonics. The heterogeneous integration of III-V semiconductor with Si cavity seems to be one of the most promising approaches. Various III-V/Si hybrid lasers have been reported, by either bonding III-V gain materials to Si or the growth of III-V materials directly on Si.

Based on the heterogeneous transfer printing process, and the bandedge effect in photonic crystal cavities, we investigate the design and fabrication of the room temperature 1550 nm long wavelength photonic crystal surface-emitting lasers (PCSEL) on SOI substrate and directly on bulk Si substrate. Single mode lasing was observed with narrowing linewidth of 0.54 nm and excellent side mode suppression ratio (SMSR) of 31.8 dB. In addition, thermal performance was also investigated to realize efficient heat dissipation and low thermal resistance afforded by the architecture of PCSEL on bulk Si substrate. The experiment results are also correlated to theoretical and numerical analysis to understand the mode properties and thermal performance.

Lateral cavity size scaling is another challenging issue for on-chip PCSELs. Typically, the PCSEL devices demonstrated so far have relatively large lateral sizes around 100 -150 μm. Such a large in-plane size (L~250a) can be regarded as an infinite structure, so the lateral loss will be very small and can be ignored. On the contrary, when the device dimension becomes smaller, the lateral loss will have significant impact on the various mode properties such as quality factor (Q), confinement factor (Γ_{QW}), side mode suppression ratio (SMSR), and gain threshold (g_{th}). Here we report the experimental and theoretical investigations of the lateral size effects associated with the finite cavity dimension based on a room temperature PCSEL on Si substrate, along with the strategies to mitigate this problem by incorporating various in-plane and vertical confinement schemes.

Finally, buried tunnel-junction (BTJ) has been employed for electrical pumping operation. The BTJ structure shows an effective lateral current confinement capability in the device. At the same time, it allows the substitution of the top p-doped layers by n-doped ones on top of the BTJ region to obtain lower electrical resistance. The electrically pumped PCSEL on Si substrate was demonstrated. The detailed design and fabrication of BTJ PCSEL were introduced, including the aperture size, current-voltage (IV) performance, process flows, and lasing characteristics.

TABLE OF CONTENTS

Acknowledgements iii

Abstract v

TABLE OF CONTENTS vii

List of Illustrations ix

List of Tables xv

Chapter 1 Introduction 1

1.1 Motivation 1

1.2 Overview of Dissertation 4

Chapter 2 Photonic Crystal Surface Emitting Lasers 5

2.1 Photonic Crystal Bandedge Effect 5

2.2 Laser Principle 8

2.3 Cavity Design 11

2.3.1 Gain Medium: InGaAsP Multi-Quantum-Well 12

2.3.2 Silicon Photonic Crystal Cavity 14

2.3.3 Cavity Resonance Modes 18

2.3.4 Mode Property 21

2.3.5 Coupling Efficiency 24

2.4 Device Fabrication 26

Chapter 3 Measurement and Lasing Characteristics 29

3.1 Micro-Photoluminescence Setup 29

3.2 Room Temperature PCSEL on SOI 30

3.3 Lateral Size Scaling of PCSEL 33

3.4 Thermal Performance of PCSEL 40

3.4.1 PCSEL on Bulk Si 40

3.4.2 Thermal Resistance 44
3.5 Discussions 48
Chapter 4 Electrically Pumped PCSEL 49
4.1 Buried Tunneling Junction and Cavity Design 49
4.2 Electrically Pumped BTJ PCSEL 53
4.2.1 Fabrication Process 53
4.2.2 Current Voltage Characteristics 58
4.3 Device Characteristics 61
4.4 Discussion and Analysis 64
Chapter 5 Concluding Remark and Future Research 67
Appendix A List of Publications 70
References 73
Biographical Information 77

List of Illustrations

Figure 2-1 (a) Lattice parameters for the square-lattice air hole PC structures are air hole radius "*r*" and lattice constant "*a*". (b) Modelled band structure of a PC consisting of circular atoms on a square lattice [34]. 5

Figure 2-2 (a) Schematic of propagating directions of coupled waves at different bandedge modes. (b) Vertical diffraction. The red arrows indicate lightwaves diffracted into the vertical (z) direction [30, 32]. 7

Figure 2-3 Optical arrangement of a distributed feedback semiconductor laser [35]. 8

Figure 2-4 (a) In-plane diffraction. The yellow arrows indicate in-plane (*x*-*y*) propagating lightwaves. The lattice constant *a* is equal to one wavelength. (b) Schematic of the PCSEL structure on GaAs substrate [32]..... 9

Figure 2-5 The schematics of the key design factors [32] 11

Figure 2-6 Temperature-dependent photoluminescence spectra of InGaAsP MQW..... 13

Figure 2-7 The scanning electron microscope images of Si-PC cavitiy designed at different parameters. (a) *a*=480, *r/a*=0.2 for PCSEL-I. (b) *a*=480, *r/a*=0.15 for PCSEL-II. (c) *a*=480, *r/a*=0.14 for PCSEL-III. 15

Figure 2-8 Reflection measurement setup for Si-PC cavity characterizations. Broadband light source is employed as the incident light which is detected by optical spectrum analyzer controlling by labview computer [37]. 16

Figure 2-9 Simulated (Sim) and measured (Mes) reflection spectra of surface normal 2D Si-PC designed for different devices. (a) PCSL-I. (b) PCSEL-II. (c) PCSEL-III. 17

Figure 2-10 (a) Schematic of hybrid III-V/Si PCSEL cavity on Si substrate, which consists of III-V active MQW structure and Si-PC cavity. (b) Cavity refractive index profile. (c) Cavity design structure of laser on SOI substrate..... 18

Figure 2-11 (a) Photonic band diagram along Γ- X direction of Si-PC bandedge laser cavity structure for PCSLE-I with normalized frequency. (b) PCSEL-II. (c) PCSEL-III.....20

Figure 2-12 Simulated cavity mode of Si-PC bandedge laser cavity structure for (a) PCSEL-I. (b) PCSEL-II. (c) PCSEL-III.....21

Figure 2-13 The simulated H-field intensity distributions of Si-PC bandedge laser cavity structure for (a) Mode A in PCSLE-I. (b) Mode C in PCSEL-II. (c) Mode D in PCSEL-III.....22

Figure 2-14 Cross section views of schematic of Si-PC bandedge laser cavity structure and field distributions in the xz plane (left) for (a) Mode A in PCSEL-I. (b) Mode C in PCSEL-II. (c) Mode D in PCSEL-III. 25

Figure 2-15 (a) A micrograph image of a fabricated Si-PC on an SOI substrate. (b) Micrograph images of 4 x 4 InGaAsP mesa on original InP substrate. (c) A micrograph image of sample covered by Apiezone wax as a protection layer. 26

Figure 2-16 Schematic of the steps to fabricate hybrid III-V/Si PCSEL on SOI substrate. 27

Figure 2-17 (a) Microscope image of 4 x 4 InGaAsP MQW membrane successfully transferred onto Si-PC cavity. (b) SEM cross-view of a InGaAsP MQW membarne transferred onto Si-PC cavity. (c) SEM top view image. (d) Measured PL spectra of the devices before and after transferred.....28

Figure 3-1 Schematic of optically pumped micro-photoluminescence (μPL) setup based on monochromater TRIAX320 spectrograph both for LT and RT measurements and a 300 mW green laser (532 nm) are employed as a pump laser [37].....29

Figure 3-2 (a) Lasing power and linewidth versus input power density at room temperature; (b) Lasing spectral output (plotted in semi-log scale) above the pumping threshold. (c) Simulated reflection spectrum (red-dashed line), the measured laser emission spectrum (solid black line), and the QW PL spectrum (blue-dashed line) for PCSEL-III at room temperature. (d) Measured polarization properties above threshold at λ = 1542 nm. 30

Figure 3-3 (a) Lasing power and linewidth versus input pump power for PCSEL-I at T = 25 K. (b) Lasing spectral output (plotted in semi-log scale) above the pumping threshold for PCSEL-I. (c) Measured polarization properties above threshold at λ = 1424 nm. (d) Lasing power and linewidth versus input pump power for PCSEL-II at T = 180 K. (e) Lasing spectral output (plotted in semi-log scale) above the pumping threshold for PCSEL-II. (f) Measured polarization properties above threshold at λ = 1505 nm. 31

Figure 3-4 (a) Simulated reflection spectrum (red-dashed line), the measured laser emission spectrum (solid black line), and the QW PL spectrum (blue-dashed line) for PCSEL-I at T = 25 K. (b) PCSEL-II at T=180 K. 32

Figure 3-5 (a) Illustration of the pumping spot size and position in the experiment, in which the device size is 300 μm x 300 μm; (c) Lasing threshold and SMSR versus pump spot size; (d) Lasing peak location and linewisth versus pumping spot size. 33

Figure 3-6 (a) Schematic of PCSEL with zero etching depth. (b) Schematic of PCSEL with 330 nm etching depth. (c) Schematic of PCSEL with 520 nm etching depth. (d) Photo image of 600 x 600 μm^2 PCSEL on Si PC cavity. (e) Photo image of PCSELs with different size at 330 nm vertical etching depth. (f) Photo image of PCSELs with different size at 520 nm vertical etching depth. 35

Figure 3-7 (a) The measured lasing threshold of three cavity schemes versus device size. (b) The measured SMSR of three cavity schemes versus device size. 36

Figure 3-8 (a) The simulated gain threshold and *Q* factor versus the different device size. (b) The simulated gain threshold and *Q* factor versus the different etching depth. 37

Figure 3-9 Schematics and simulated field distributions of PCSEL cavity with enhanced lateral and vertical confinements. 39

Figure 3-10 (a) Schematic of PC bandedge membrane laser on bulk Si substrate. (b) Cavity refractive index profile. (c) Cavity design structure of laser on bulk substrate. 41

Figure 3-11 (a) Zoomed-in SEM top view of the defect-free Si-PC cavity on bulk Si substrate. (b) Cross-sectional view of a InGaAsP membrane integrated with Si-PC on bulk Si substrate. (c) Field distribution of cavity mode. 42

Figure 3-12 (a) Lasing power and linewidth versus input power density at T=160 K for PCSEL on bulk Si substrate. (b) Emission spectrum of the laser above threshold. (c) Simulated reflection spectrum (red-dashed line), the measured laser emission spectrum (solid black line), and the QW PL spectrum (blue-dashed line) for PCSEL on bulk Si at T=160 K. (d) Measured polarization properties above threshold at λ = 1452 nm. 43

Figure 3-13 (a) Lasing spectra at different pump powers above threshold at constant 160 K. (b) Lasing spectra at different operation temperatures with constant 40 mW pump power. 45

Figure 3-14 (a) Emission peak wavelength shift versus pump powers for PCSEL on SOI and on bulk Si substrate. (b) Emission peak wavelength shift versus operation temperatures for PCSEL on SOI and on bulk Si substrate. 46

Figure 3-15 (a) Schematic of the PCSEL on SOI substrate. (b) Schematic of the PCSEL on bulk Si substrate. (c) Thermal field distributions of PCSEL on SOI substrate with 400 nm BOX. (d) Thermal field distributions of PCSEL on bulk Si substrat. 47

Figure 4-1 (a) Schematic of a electrically pumped BTJ PCSEL on Si substrate. (b) Key design parameters of InGaAsP QW cavity with embedded BTJ region on SOI substrate. 50

Figure 4-2 Schematic view of a BTJ PCSEL (a) 1^{st} growth (b) BTJ region definition (c) 2^{nd} regrowth. 51

Figure 4-3 Schematic of the steps to fabricate electrically pumped BTJ PCSEL. 54

Figure 4-4 Fabricated 4 x 4 electrically pumped BTJ PCSELs on Si substrate. (a) InGaAsP membrane transferred printing on Si-PC cavity. (b) After top metal contact. (c) After bottom metal contact. (d) After SiO_2 passivation. (e) Interconnector. (f) Packaging and wire bonding. 57

Figure 4-5 (a) I-V curves of devices with different BTJ dimension in linear scale. (b) Log scale. 59

Figure 4-6 (a) Ideality factory - BTJ dimension relationship of the applied bias at 1V. (b) Dark current with respect to different BTJ dimension at -0.8V biased current. 60

Figure 4-7 (a) Optically pumped lasing spectra from our BTJ PCSEL as a function of optical pumping power at room temperature. (b) Emission spectrum of the laser above threshold. 61

Figure 4-8 (a) Electrically pumped lasing spectra from a 50 x 50 μm^2 BTJ PCSEL device at different bias current level. (b) Zoom-in view of bias current at 0.05 mA to 5 mA. (c) L-I characteristics and linewidths versus the bias current. (d) C.W. L-I-

V characteristics of the BTJ PCSEL. The ridge of the BTJ dimension is 50 μm in both width and length. 62

Figure 4-9 (a) A measured output spectrum at an injection current of 10 mA, which shows a side mode suppression ratio of about 10.1dB. (b) Measured polarization properties above threshold at λ = 1,504 nm. 63

Figure 4-10 (a) Micrographs of a 4x4 array of electrically pumped BTJ PCSEL. (b) Overall view of device image captured from IR camera. (c) Zoom-in view of the 2D beam profile from device M22 with 50 x 50 μm^2 BTJ dimension. 65

Figure 4-11 (a) Fano/guided resonance modes of the BTJ PCSEL cavities. (b) Field distribution of mode B from BTJ PCSEL at room temperature operation. 66

List of Tables

Table 2-1 Key Design Parameters of InGaAsP MQW Cavity on InP Substrate 12

Table 2-2 Parameters of 2D square lattice PC for three operations temperatures. 15

Table 2-3 Key design parameters of InGaAsP QW cavity on SOI Substrate for three operations temperatures. 19

Table 2-4 The calculated values of the quantities Γ_{QW}, Q, α and g_{th}. 23

Table 3-1 Cavity Design Structure of Laser on Bulk Si and SOI 44

Table 4-1 Cavity Design Structure of electrically pumped BTJ PCSEL on Si substrate .. 52

Chapter 1 Introduction

1.1 Motivation

Significant progresses have been on silicon (Si) photonics. The main motivations for integration of electronics and photonics on Si are performance and cost of devices. It is very well known that Si is an indirect band gap material and not efficient to emit light compared to other direct band gap III-V materials. In this regard, many researchers have focused their attentions on the realization of Si-based optoelectronic devices. In recent years, remarkable achievements have been obtained from Si photonics research on various passive devices [1-3], optical modulators [4, 5], and optical detectors [6-8]. However, the realization of practical light sources on Si substrates remains a major barrier in the generation of Si-based integrated photonics and electronics in large volumes and at low cost.

Promising performances have been reported for Si-based lasers, which are fabricated by the direct growth of III–V materials on Si [9-11]. However, the results of reliability are still a problem due to lattice mismatch and thermal expansion mismatch of those III-V materials and Si. Bonding is an effective and practical method in this field which solves the problem of lattice mismatch between different materials resulting from direct epitaxial growth. Several bonding methods have been reported, including direct bonding [12], adhesive bonding [13], metal bonding [14], etc. However, direct bonding requires a chemically ultraclean and atom scale smooth surface, adhesive bonding usually introduces an electrical insulating layer resulting in low thermal conductivity, and the weakness of metal bonding is that there is strong light absorption by the metal between the two parts being bonded. Another approach to integrate III-V materials to Si is transfer printing technique [15-17]. A lot of impressive devices have been successfully fabricated with this method [18-21]. Also, it provides an easy and effective way to make a

large-scale integration of III-V lasers on Si [22]. By employing well developed transfer printing technique for heterogeneous integration, our motivation is to demonstrate the Si based lasers for 1550 nm wavelength communication application.

Most lasers demonstrated in the near infrared wavelength range so far are edge-emitting lasers, the dominant light sources used in high speed, high capacity wavelength-division multiplexing (WDM) optical communication systems, owning to its excellent high power operation and stable single mode spectral properties especially in distributed feedback (DFB) laser cavities. On the other hand, vertical-cavity surface-emitting lasers (VCSELs) also exhibit advantageous properties, such as circular beam shape, catastrophic optical damage free, and two-dimensional integration capabilities with complementary metal-oxide-semiconductor (CMOS) electronics. However, its relatively low output power and poor spectral properties are largely limited to applications in communication, computing, and consumer electronic systems.

Recently, photonic crystal surface-emitting lasers (PCSELs) are attracting great attention, where the bandedge effect was utilized in defect-free two-dimensional (2D) photonic crystal (PC) structures [23-31]. Due to the 2D of such devices, the Bragg diffraction that occurs is multidirectional. This is physically very interesting because multidirectional Bragg diffraction may be able to yield coupling mechanisms similar as the principle of traditional DFB lasers, possibly leading to achieve high performance semiconductor surface emitting lasers, including low lasing threshold, single longitudinal and transverse mode over a large lasing area, narrow linewidth, high power output, small beam divergence angle, polarization control, and output beam pattern control. Based on the bandedge effect, high performance PCSEL on GaAs has been demonstrated, including a very recent demonstration of high power, single mode, and large area PC

bandedge lasers with unpatterned quantum well (QW) active region using a regrowth process [32].

Based on the membrane transfer printing technique for heterogeneous integration of III-V with Si materials, we report here the design and demonstration of PCSEL on Si substrate. In addition, the lateral size effect and thermal property of hybrid III-V/Si PCSEL was analyzed based on the experimental and theoretical investigations. We also propose the strategies to mitigate the lateral loss by incorporating supplementary in-plane and vertical confinement schemes.

Another motivation is the experimentally demonstration of the electrically pumped operation PCSEL on Si substrate. Buried tunnel-junction (BTJ) have been widely used for long-wavelength membrane light source, which presented a wide various of features, such as highly strained active region, highly doping levels for reduced intrinsic parasitics, and high speed application. By employing BTJ structure as a current spreading control, the hybrid III-V/Si BTJ PCSEL was demonstrated under room temperature operation. This demonstration promises a hybrid 1,550 nm emission wavelength laser sources on Si towards three-dimensional (3D) integrated Si photonics for on-chip WDM systems for a wide range of volume photonic/electronic applications in computing, communication, sensing, imaging, etc.

1.2 Overview of Dissertation

Chapter 2 begins with presenting an introduction to bandedge effect in PC and the laser principle, followed by the investigation of cavity mode properties and simulation. Then, the fabrication details for a room temperature hybrid III-V/Si PCSEL is discussed, followed by the description of transfer printing technique.

Chapter 3 first presents the micro-Photoluminescence setup. Consequently, room temperature operation lasing characteristics were discussed. The experimental results are correlated to theoretical and numerical analysis. Next, the lasing threshold dependent on cavity dimension was investigated by tuning the incident spot size and shrinking the device size. Finally, the thermal performance was also investigated to realize efficient heat dissipation and low thermal resistance afforded by the architecture of PCSEL directly built on bulk Si substrate.

Chapter 4 begins with the introduction of BTJ QW structure, followed by the investigation of current injection mechanism and current voltage propertied. Then, the fabrication processes of electrically pumped BTJ PCSEL were discussed. Next, the cavity properties and lasing characteristics of an electrically pumped hybrid III-V/Si PCSEL were discussed. Finally, the measured EL spectrum and simulated spectrum are compared and analyzed.

Finally, concluding remarks and future research direction are presented in Chapter 5.

Chapter 2 Photonic Crystal Surface Emitting Lasers

2.1 Photonic Crystal Bandedge Effect

In a photonic crystal (PC) the periodic variation in refractive index determines the propagation of photons. By solving Maxwell's equations [33] it is possible to plot the photonic band structure which is similar to a semiconductor electronic band structure showing the allowed photonic energy levels as a function of wave vector. A two-dimensional (2D) PC is periodic along two of its axes and homogeneous along the third axis. A typical specimen, consisting of a square lattice of circular air hole is shown in Figure 2-1(a), where *r* and *a* represent to air hole radius and lattice constant, respectively. By using the rigorous coupled-wave analysis (RCWA) techniques, the simulated photonic band structure of a 2D PC with circular air hole square lattice is shown in Figure 2-1(b).

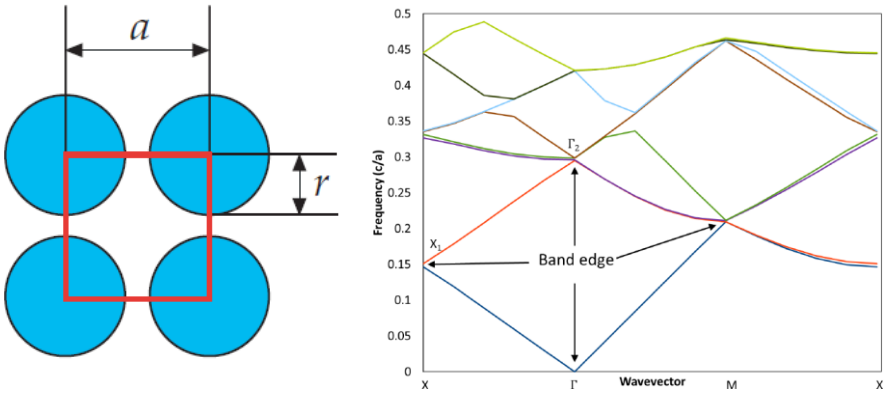

(a) (b)

Figure 2-1 (a) Lattice parameters for the square-lattice air hole PC structures are air hole radius "*r*" and lattice constant "*a*". (b) Modelled band structure of a PC consisting of circular atoms on a square lattice [34].

In a photonic band structure a bandedge is a region where the gradient is zero. At this point, waves propagate in different coupling direction and significantly increase the mode density. It is particularly interesting that each of these points exhibits a different

type of wave coupling according to the Bragg conditions. Figure 2-2(a) shows the propagating directions of coupled waves at different bandedge modes. Point X1 corresponds to the coupling of only two waves, those propagating in the forward and backward directions. This coupling is similar to that of a conventional distributed feedback (DFB) laser. However, as there are four equivalent Γ-X directions in the structure, a cavity can exist independently in each of the four different directions, forming four independent lasers. Point Γ2 has a unique coupling characteristic, when the wave propagates in the +y direction (0°), it is reflected backwards because the second-order Bragg diffraction condition is satisfied. In addition, the wave is also diffracted to the perpendicular directions (+90° and -90°) because the first-order Bragg diffraction conditions are satisfied for these directions, and these diffracted waves are again reflected backwards. Consequently, waves propagating in four directions are coupled with each other, and a 2D standing wave state is formed in the PC plane. Furthermore, the in-plane wave in resonance is also diffracted toward the vertical (z) direction due to the first-order Bragg diffraction condition, as shown in Figure 2-2(b).

There are many other points where waves are multi directionally coupled in plane and out of plane. However, the angles of out-of-plane coupling by Bragg diffraction either vary from 90° entirely or have a component that varies from 90°, i.e., light is also coupled out of plane at an angle other than 90°. For example, at point Γ3, light is coupled out of plane at an angle of 54.7° ~diffraction to as well as at 90°. Therefore, we consider that the point offering the most desirable characteristics is point Γ2.

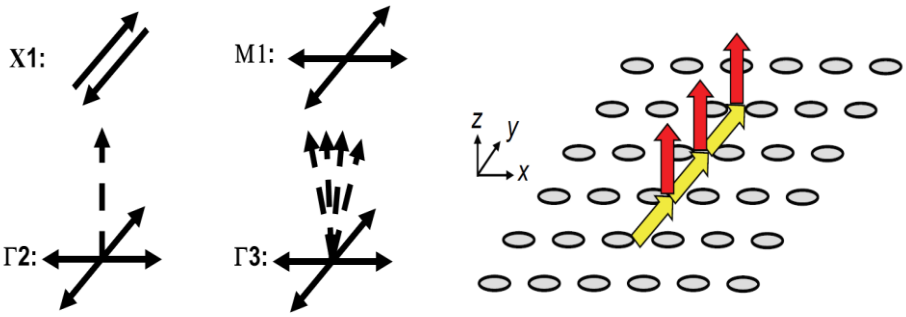

Figure 2-2 (a) Schematic of propagating directions of coupled waves at different bandedge modes. (b) Vertical diffraction. The red arrows indicate lightwaves diffracted into the vertical (z) direction [30, 32].

`

2.2 Laser Principle

The original concept for 2D photonic crystal surface emitting laser (PCSEL) is from conventional one-dimensional (1D) grating DFB laser. A DFB laser is a laser where the resonator consists of a periodic structure, which acts as a distributed reflector in the wavelength range of laser action, and contains a gain medium. This structure is essentially the combination of optical gain within the Bragg gratings as shown in Figure 2-3. The device has multiple resonator modes, but there is typically one mode which is favored in terms of losses. Therefore, single mode operation is often easily achieved over large device size.

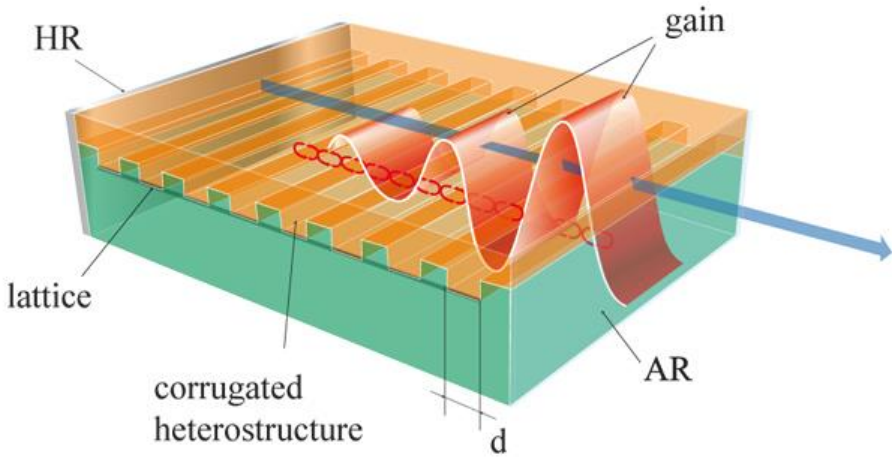

Figure 2-3 Optical arrangement of a distributed feedback semiconductor laser [35].

In previous section, 2D PC bandedge effect was introduced. Figure 2-4(a) shows a schematic of diffraction of light waves in a 2D square-lattice PC. The group velocity of light wave is zero so that it forms a standing wave at bandedge point. The symmetry of the square lattice PC results in four equivalent Γ-X directions. When light having wavelength equal to the lattice constant propagates in one Γ–X direction, it is diffracted

not only backward (0^o, 180^o), but also in the other two equivalent Γ-X directions (90^o, -90^o). Thus, light wave propagating in four equivalent directions is coupled and as a result a standing wave is formed in the 2D PC. Light is also diffracted in a direction normal to the PC plane due to first-order Bragg diffraction.

In order to create a laser cavity, the 2D patterned square-lattice PC layer is placed close to the gain medium. Although the light is confined to the region close to the gain medium, the evanescent wave still penetrates into the PC layer. Here, the pitch of the square-lattice PC is designed to match to the wavelength of the light propagating in the gain medium. In this case, the propagating light inside the PC layer will undergo multiple Bragg diffraction.

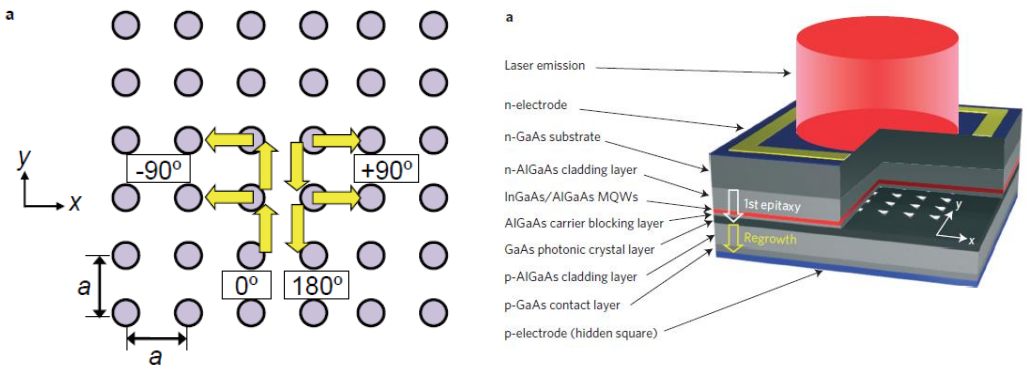

(a) (b)

Figure 2-4 (a) In-plane diffraction. The yellow arrows indicate in-plane (*x*-*y*) propagating lightwaves. The lattice constant *a* is equal to one wavelength. (b) Schematic of the PCSEL structure on GaAs substrate [32].

Based on the bandedge effect, a promising route towards realizing a single longitudinal-transverse mode with high power and high beam quality utilizes a PCSEL is attracting a great deal of attention. In addition, because they demonstrate large-area coherent lasing, resulting in a narrow, single-lobed beam. PCSELs are also attractive as

versatile, single-chip light sources with the capability to control the polarization, beam pattern and beam direction, and to generate vector beams. Recently, high performance lasers on GaAs has been demonstrated, including a very recent demonstration of high power, single mode, large area PC bandedge lasers with unpatterned quantum well (QW) active region using a regrowth process. Figure 2-4(b) presents a schematic structure of the PCSEL developed in the work of Noda in Japan [32].

2.3 Cavity Design

In order to achieve room-temperature operation in PC bandedge membrane lasers in such a cavity, it is highly desirable to design a cavity with the following aspects: (1) Two-dimensional Si photonic crystal; (2) Hybrid InGaAsP/Si Cavity; (3) Bandedge mode design; (4) Bragg Diffraction; (5) Sufficient cavity confinement factor; (6) Strong in-plane coupling. The schematics of the key design factors are shown in Figure 2-5. The detail design strategies will be discussed in following sections.

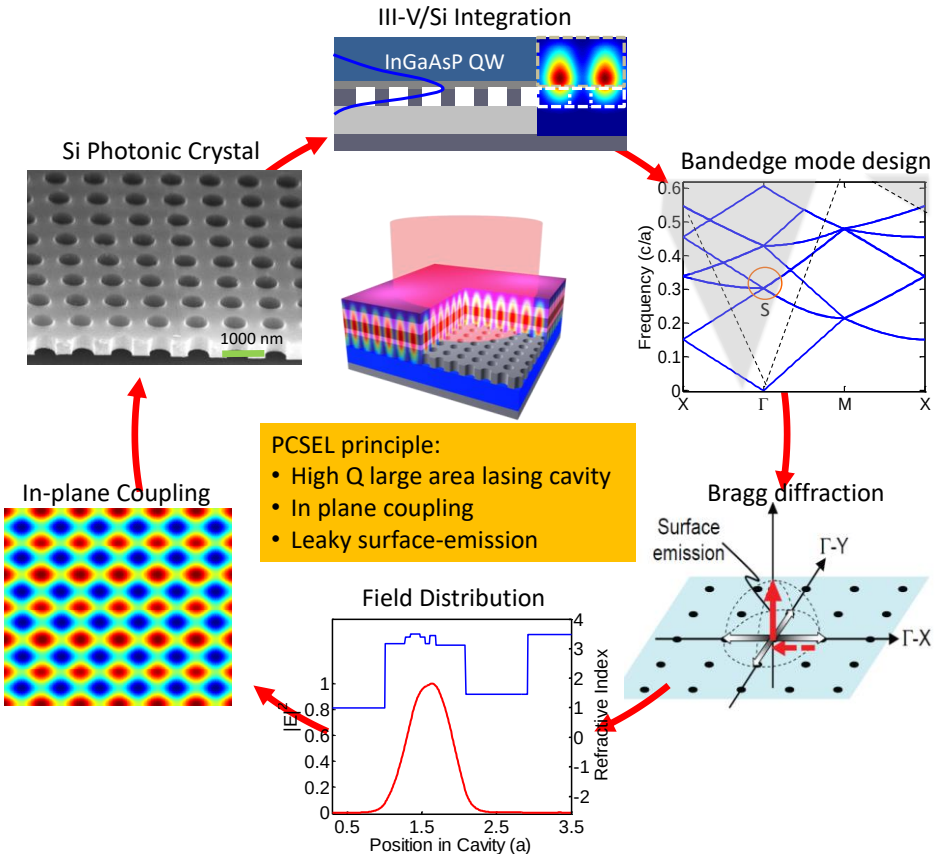

Figure 2-5 The schematics of the key design factors [32]

2.3.1 Gain Medium: InGaAsP Multi-Quantum-Well

The whole InGaAsP multi-quantum-well (MQW) structure was grown on (001) n-InP substrate by metal-organic chemical vapor deposition (MOCVD), consisting of top and bottom InGaAs contact layer, top and bottom InP cladding layers, and eight pairs of strain-compensated $In_{0.76}Ga_{0.24}As_{0.83}P_{0.17}/In_{0.485}Ga_{0.515}As_{0.83}P_{0.17}$ with the center emission wavelength of 1,535 nm at room temperature. A InGaAs/InP sacrificial bilayer was grown first on InP substrate for selective wet-etching and substrate removal. The detail layer description, thickness, doping concentration, and refractive index are shown in Table 2-1.

Table 2-1 Key Design Parameters of InGaAsP MQW Cavity on InP Substrate

Layer	Description	Material	Thickness (nm)	Dopant	Doping (cm^{-3})	Optical Index	Optical Thickness
23	Contact layer	InGaAs	40	Zn	1e19	3.444	0.0889
22	Cladding layer	InP	50	Zn	2e18	3.172	0.1023
21	Spacer layer	InP	81.5	Undoped (UID)		3.172	0.16679
20	Barrier (0.9% ts)	$In_{0.485}Ga_{0.515}As_{0.83}P_{0.17}$	7.5	Undoped (UID)		3.4	0.0165
5…19	Quantum wells (1% cs) (x8)	$In_{0.76}Ga_{0.24}As_{0.83}P_{0.17}$	7.5	Undoped (UID)		3.5	0.1355
4…18	Barrier (0.9% ts) (x8)	$In_{0.485}Ga_{0.515}As_{0.83}P_{0.17}$	7.5	Undoped (UID)		3.4	0.1316
3	Spacer layer	InP	21.5	Undoped (UID)		3.172	0.16679
2	Cladding layer	InP	10	Si	2e18	3.172	0.1023
1	Contact layer	InGaAs	40	Si	1e19	3.444	0.0889
	Sacrificial layer	InP	100	Si	5e18		
	Sacrificial layer	InGaAs	500	Si	5e18		
InP Substrate (n+)							

Figure 2-6 shows the temperature-dependent photoluminescence (PL) response for InGaAsP MQW. The figure exhibits that the PL peak energy of the InGaAsP MQW shows an apparent dependence on temperature. The PL peak wavelength initially located at 1,535 nm at room temperature and it gradually blue shifts with decreasing temperature. The peak location is observed at 1,430 nm as temperature down to 25 K. The peak shift versus temperature is also numerically calculated, where the MQW

emission peak locations dependent on temperature at a rate of $\Delta\lambda/\Delta T$, close to the value of 0.4 nm/K [36].

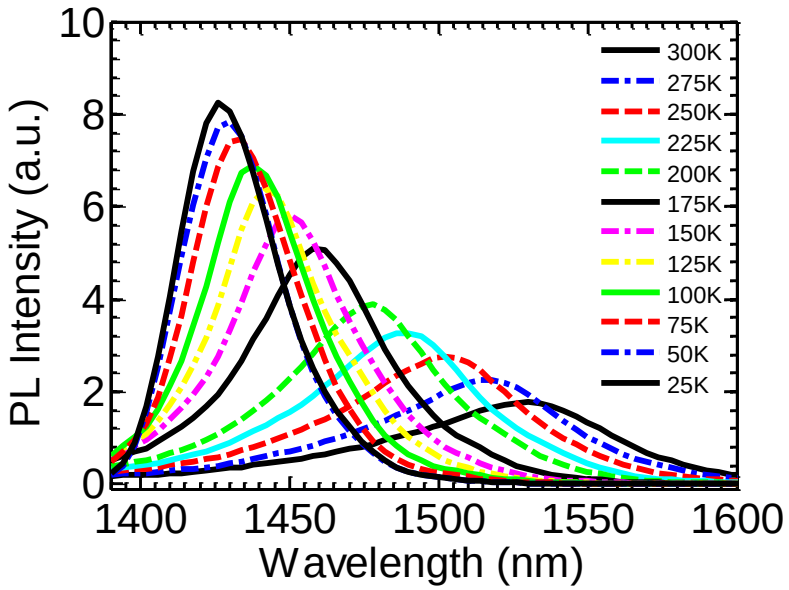

Figure 2-6 Temperature-dependent photoluminescence spectra of InGaAsP MQW.

2.3.2 Silicon Photonic Crystal Cavity

Silicon photonic crystal (Si-PC) cavity was designed and fabricated on a silicon-on-insulator (SOI) substrate. The 340 nm thick top Si layer has two parts consisting of Si with the index of refractive taken to be 3.48 and air hole with the index of refractive of 1.0, following layer is a buried oxide (BOX) of 400 nm with the index of refractive of 1.48. For simplicity, it is assumed that Si-PC cavities are infinitely periodic lattice dielectric, and materials are non-dispersive and lossless in our 1,550 nm photonic crystal surface emitting laser PCSEL of interest.

The key design parameters of our two dimensional (2D) Si-PC square lattice consists of refractive index (*n*), slab thickness (*t*) of top Si layer, lattice constant (*a*), and air hole radius (*r*). By optimizing these design parameters, it is possible to have the resonance modes located in the 1,400 to 1,600 nm wavelength range. Here the refractive indices of Si and SiO_2 are constant as mentioned earlier and slab thicknesses of top Si and buried oxide layers also have been fixed in our case. Therefore, the remaining two parameters which are lattice constant and air hole radius will play the important roles in designing the resonances distribution in the cavity.

In our experiment, three devices operating at different temperatures are designed. The PL peak energy gradually increases with the decreasing temperature. We start from low temperature design with high PL energy and move to higher temperature, which shows great improvement of the lasing opportunity on the same platform. Total thicknesses of the top Si layer cavity, lattice constant, and air hole size vary for three device designs operating at different temperatures are shown in the Table 2-2, denoted by PCSEL-I, PCSEL-II, and PCSEL-III, respectively. The lattice constant for the square lattice air hole Si-PC lattice is chosen to be a = 480 nm to match with the second order Bragg diffraction equation. In addition, the air hole radius are designed to match InGaAsP

MQW emission peak locations at different operation temperatures with *r*=0.2, *r*=0.15, *r*=0.14, respectively.

Table 2-2 Parameters of 2D square lattice PC for three operations temperatures.

Layer materials	PCSEL-I (25K)	PCSEL-II (180K)	PCSEL-III (300K)	Refractive index
Si-PC	120 nm, r/a=0.2	230 nm, r/a=0.15	190 nm, r/a=0.14	3.3
SiO_2	400 nm			1.449
Si substrate	525 μm			3.48

The top Si layer was first thinned down based on thermal oxidation and selective wet etching processes from 230 nm to 120 nm, 230 nm (no change), and 190 nm for PCSEL-I, PCSEL-II, and PCSEL-III, respectively. Pattern was defined in positive electron beam resist ZEP520A using electron beam lithography (EBL; Joel JBX6000 system), and directly transferred into top Si layer using chemistry reactive ion etching (RIE; Plasma-Therm's 790 series, 168 W RIE power, pressure 35 mTorr, 25.4 sccm gas flow rate Hbr, 4.0 sccm gas flow rate Cl_2; etching time 6 minutes). Figure 2-7(a)-(c) show the scanning electron microscopy (SEM) images of top view of Si-PC fabricated on SOI substrate with the high quality patterning and etching which play an important role in achieving the very good lasing characteristics of PCSEL.

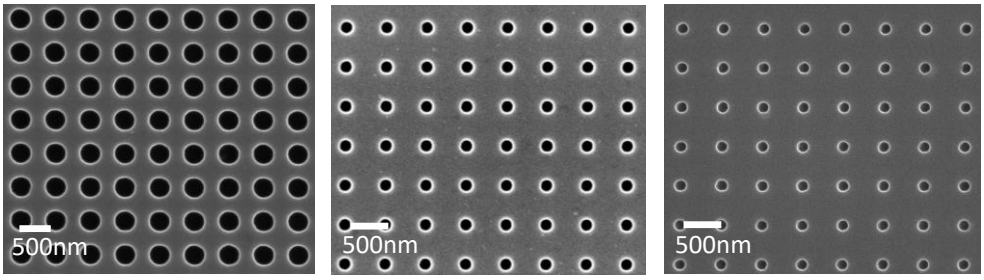

Figure 2-7 The scanning electron microscope images of Si-PC cavitiy designed at different parameters. (a) *a*=480, *r/a*=0.2 for PCSEL-I. (b) *a*=480, *r/a*=0.15 for PCSEL-II. (c) *a*=480, *r/a*=0.14 for PCSEL-III.

The reflection spectra from these three Si-PC cavities are measured to investigate the optical performance and device quality. Figure 2-8 shows the schematic of reflection measurement setup where an unpolarized broadband tungsten halogen light sources was collimated and focused into a small spot size with an objective lens. By precisely controlling the sample holder, we can perform the reflection measurement. The reflected light was detected by optical spectrum analyzer (OSA) and processed by LABVIEW software.

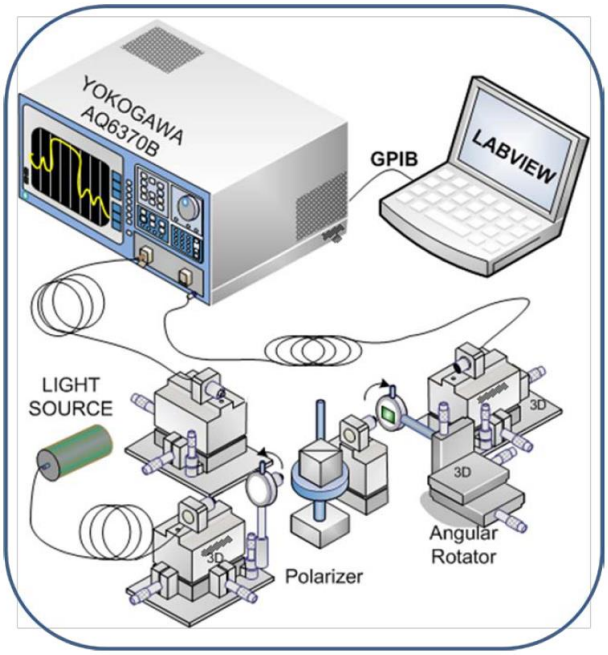

Figure 2-8 Reflection measurement setup for Si-PC cavity characterizations. Broadband light source is employed as the incident light which is detected by optical spectrum analyzer controlling by labview computer [37].

The 2D Si-PC designed for PCSEL-I is shown in Figure 2-9(a) where blue curve shows the simulated result (Sim) and red-dash curve exhibits the measured result (Mes). The simulation results are based on Stanford Stratified Structure Solver (S_4) software package simulation technique [38]. The measured and simulated reflection spectra are

shown in Figure 2-9(b) and (c), for PCSEL-II and PCSEL-III, respectively. Some degradation is evident in the measured reflection spectra of PCSEL-III, mostly due to certain fabrication non-uniformity associated with the large area photonic crystal structure on SOI substrate. Spectral shift is also observed from the PCSEL-I and PCSEL-II, mostly due to the imperfect sidewall and relatively larger air hole radius at surface. The measured spectra of Si-PC cavities overall agree well with the simulated results.

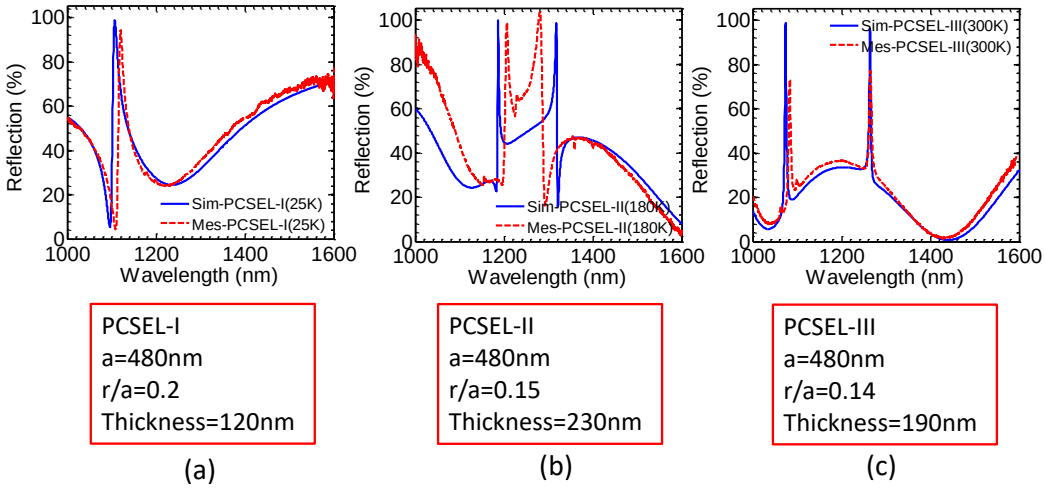

Figure 2-9 Simulated (Sim) and measured (Mes) reflection spectra of surface normal 2D Si-PC designed for different devices. (a) PCSL-I. (b) PCSEL-II. (c) PCSEL-III.

2.3.3 Cavity Resonance Modes

A schematic of the PCSEL on Si is shown in Figure 2-10(a). The laser cavity consists of an InGaAsP MQW membrane heterostructure, and a Si-PC slab on SOI substrate with BOX layer thickness of 400 nm. The InGaAsP MQW consists of a bottom InGaAs contact layer, top and bottom InP cladding layers, and eight pairs of strain compensated $In_{0.76}Ga_{0.24}As_{0.83}P_{0.17}/In_{0.485}Ga_{0.515}As_{0.83}P_{0.17}$ with the center emission wavelength of 1535 nm at room temperature [39-41].

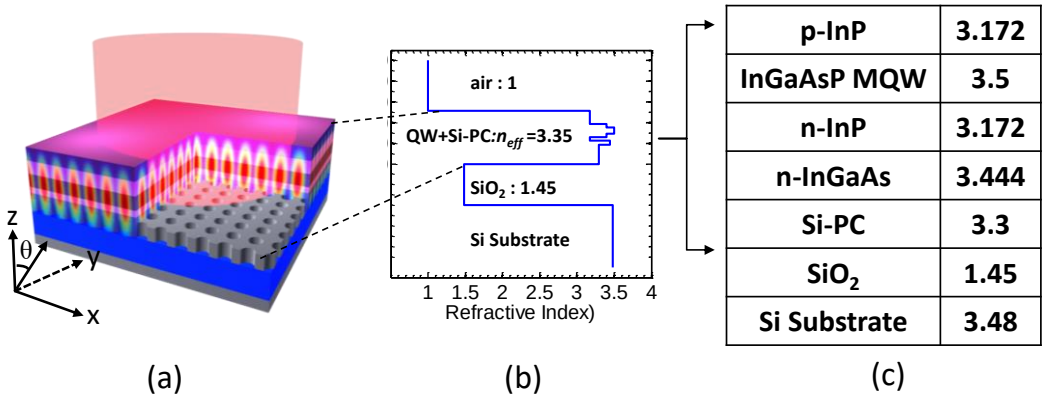

p-InP	3.172
InGaAsP MQW	3.5
n-InP	3.172
n-InGaAs	3.444
Si-PC	3.3
SiO_2	1.45
Si Substrate	3.48

Figure 2-10 (a) Schematic of hybrid III-V/Si PCSEL cavity on Si substrate, which consists of III-V active MQW structure and Si-PC cavity. (b) Cavity refractive index profile. (c) Cavity design structure of laser on SOI substrate.

The approximate refractive index n_{eff} of the whole cavity (InGaAsP MQW active layer and Si-PC) is around 3.2 based on the average dielectric constant in the initial design. Figure 2-10(b) shows the refractive index versus vertical position in the cavity. The cavity was cladded by top and bottom low refractive index layers to obtain sufficient confinement factor. Figure 2-10(c) shows the refractive index for each layer. In the case of PCSEL-III operating at room temperature, to achieve surface-emitting output for the emission wavelength close to the communication wavelength range of 1550 nm, the lattice constant *a* of the cavity is calculated to be 480 nm according to second Bragg diffraction condition $a = \lambda/n_{eff}$. Second, the air hole radius is designed to be 68 nm (r=

0.14a) in order to reduce the vertical radiation loss to obtain high *Q* and low threshold. Finally, to optimize the cavity mode match with the MQW emission peak, the thickness of the Si-PC slab is chosen to be around 190 nm.

The thicknesses of each layer of the InGaAsP MQW membrane and the parameter of Si-PC for PCSEL-I, PCSEL-II, and PCSEL-III are listed in Table 2-3. To match the cavity mode with the MQW emission peak, the PCSEL cavity structure parameters are optimized by simulating the resonance modes of the cold cavities. All the spectral simulations are employed by using the Fourier Modal Method with Stanford Stratified Structure Solver (S_4) software package [38], In the simulation, a periodic boundary condition is used since the cavity in-plane size is over 100 μm, which can be regarded as infinity.

Table 2-3 Key design parameters of InGaAsP QW cavity on SOI Substrate for three operations temperatures.

Layer materials	PCSEL-I (25K)	PCSEL-II (180K)	PCSEL-III (300K)	Refractive index
***p*-InGaAs**	**40 nm**			**3.444**
p-InP	**130 nm**			**3.172**
InGaAsP MQW	**127 nm**			**3.5**
***n*-InP**	**130 nm**	**0**	**31 nm**	**3.172**
***n*-InGaAs**	**0**	**0**	**40 nm**	**3.444**
Si-PC	**120 nm, r/a=0.2**	**230 nm, r/a=0.15**	**190 nm, r/a=0.14**	**3.48**
SiO_2	**400 nm**			**1.449**
Si substrate	**525 μm**			**3.48**

The photonic bands of the real devices are calculated from the Fano/guided resonances peaks or dips in the simulated reflection spectra according to the relation between in-plane wave vector k// and the incident angle θ, $k// = 2\pi / \lambda \cdot \sin\theta$, where λ is the wavelength in free space. Figure 2-11(a)-(c) show the eight bands in a small in-plane

wave vector *k//* range from 0 to ~0.01 (*2π /a*) with blue-solid lines for the transverse electric (TE, s) and red-dashed lines for the transverse magnetic (TM, p) polarizations, for PCSEL-I, PCSEL-II, and -III respectively. For θ = 0°, the non-degenerate modes at Γ point are obtained from spectra of the incident angle θ = 0.01° because the non-degenerate modes cannot be directly excited by the outside normal incident light due to the symmetric property. One can clearly see the flat bands close to Γ point and the larger mode separation for the non-degenerate TM modes, ~0.005 in PCSEL-I, and 0.013 in PCSEL-II and PCSEL-III. By comparing with the mode separation in the thicker cavity, the larger mode separation in PCSEL-I is due to the high contrast refractive index to the surrounding. On the other hand, the index contrast is further increased by using thick Si-PC and thinner active layer in PCSEL-II or PCSEL-III so that the mode separation is enlarged further by comparing with PCSEL-I. Therefore, single mode lasing are easily achieved in this kind of PCSEL cavities. From the Figure 2-11, we can particularly observe all of these bands are very flat at the edges close to Γ point, which indicates very small group velocity and longer light-matter interaction time for these bandedge modes.

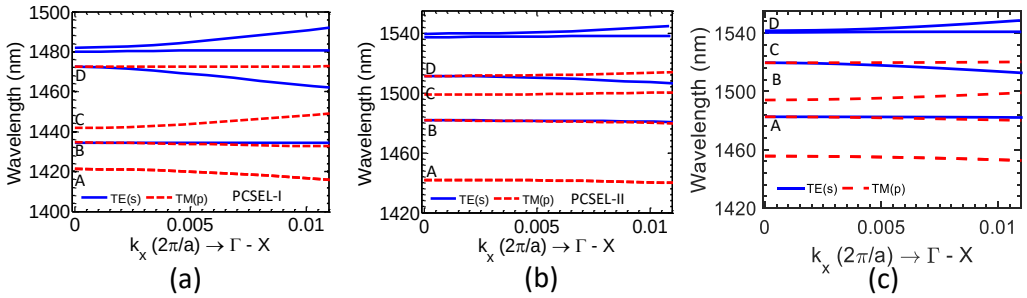

Figure 2-11 (a) Photonic band diagram along Γ- X direction of Si-PC bandedge laser cavity structure for PCSLE-I with normalized frequency. (b) PCSEL-II. (c) PCSEL-III.

2.3.4 Mode Property

To better understand the underlying physics of these three PCSEL devices, the mode properties in the cavities are correlated to theoretical and numerical analysis. Here the mode distributions in three cavities were simulated based on the parameters in the Table 2-3. Figure 2-12(a)-(c) show the simulated reflection spectra for PCSEL-I, PCSEL-II, and PCSEL-III, respectively (the incident angle θ = 0.2° is used here).

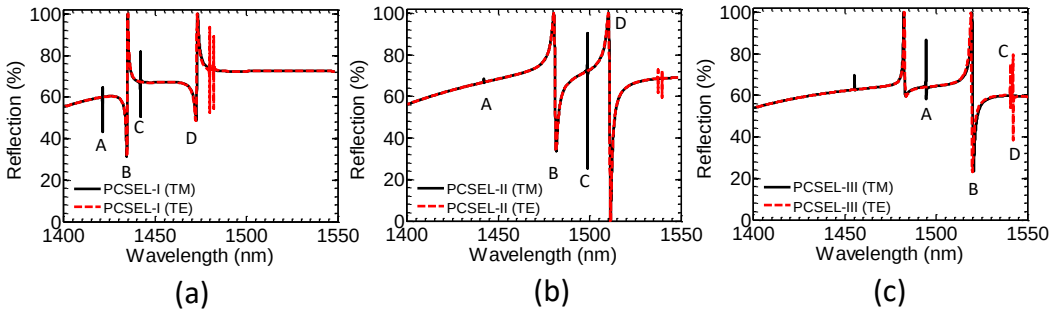

Figure 2-12 Simulated cavity mode of Si-PC bandedge laser cavity structure for (a) PCSEL-I. (b) PCSEL-II. (c) PCSEL-III.

Next, various mode properties are calculated theoretically. We will focus on resonance modes close to designed wavelength according to operation temperature. First, the quality factor (Q) is obtained by Fano fitting the guided resonances in reflection spectra [34]. Since the device is large enough with the size around 150 μm × 150 μm, which is more than 300a × 300a, it can be assumed that the edge scatting is not the dominating loss. In regarding to the cavity loss, here only the radiation loss is considered for the infinite cavity with the relationship in following:

$$\alpha = \frac{2\pi}{Q \bullet a} \tag{1}$$

The field profiles of mode A from PCSEL-I, mode C from PCSEL-II, and mode D from PCSEL-III are plotted in the Figure 2-13(a)-(c), respectively, where the integrated H-field and E-field intensity of the whole cavity along the z-axis direction are plotted together with

the cavity index profile. One can see the field is strongly confined inside the hybrid III/Si-CP cavity due to high index contrast below and above the laser cavity. The confinement factor for the TE band and TM modes are calculated according to the equation in following:

$$\Gamma_{QW} = \frac{\int_{QW} E^2 \bullet dv}{\int_{cav} E^2 \bullet dv} \tag{2}$$

$$\Gamma_{QW} = \frac{\int_{QW} H^2 \bullet dv}{\int_{cav} H^2 \bullet dv} \tag{3}$$

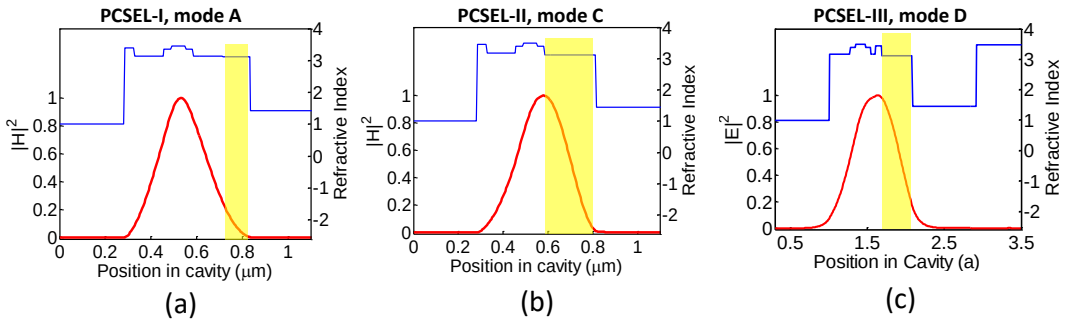

Figure 2-13 The simulated H-field intensity distributions of Si-PC bandedge laser cavity structure for (a) Mode A in PCSLE-I. (b) Mode C in PCSEL-II. (c) Mode D in PCSEL-III.

The E-field and H-field of the standing-wave distribution is demonstrated with a red line, and the cavity index profile is plotted with a blue line. Therefore, the gain threshold can be derived as follows:

$$g_{th} = \frac{\alpha}{\Gamma_{QW}} \tag{4}$$

Further information on the calculation can be found in the Table 2-4. From the table, we know the final laser oscillation for each cavity is expected to occur at the mode A (PCSEL-I) with the lowest gain threshold. In addition, we observed the mode C in PCSEL-II lases and mode D in PCSEL-III, while in PCSEL-III, the lasing is mode D, due to the lower gain threshold of resonance mode. Indeed, each mode is possible to achieve lasing once the pumped energy over threshold. The reason we investigate the mode properties is to understand the relative gain threshold from the cold cavity, which helps us easily to identify and compare the measured spectra during the device characterization.

Table 2-4 The calculated values of the quantities Γ_{QW}, Q, α and g_{th}.

Device	Mode	Γ_{QW} (%)	Q	α (cm^{-1})	g_{th} (cm^{-1})
PCSEL-I (25K)	A	24.4	5.86e5	0.22	0.92
	B	19.7	3.49e3	37.5	190.4
	C	21.7	8.67e4	1.51	6.96
	D	17.3	1.70e3	76.96	444.9
PCSEL-II (180K)	A	23.64	3.45e5	0.38	1.61
	B	19.85	1.69e3	77.5	390.4
	C	20.6	1.67e5	0.78	3.79
	D	18.5	1.32e3	99.2	536.2
PCSEL-III (300K)	A	10.0	1.81e3	71.8	718.0
	B	17.31	2.02e3	64.4	372.3
	C	16.97	1.60e5	0.81	4.77
	D	16.83	1.90e5	0.68	4.04

2.3.5 Coupling Efficiency

In particular, optical coupling phenomena in laser cavity are also investigated. The coupling coefficient for circular holes is expressed approximately as follows [30]:

$$\kappa \sim \frac{\pi \bullet \Gamma_{PC}}{a \bullet n_{eff^2}} (\varepsilon_{Si} - \varepsilon_{air}) \quad (5)$$

From this equation, we realize that the coupling efficient shows proportional to the confinement factor of Si-PC (Γ_{PC}). The calculated confinement factors of Si-PC for PCSEL-I, PCSEL-II, and PCSEL-III are 4.56%, 46%, and 37.7%, respectively. Here we discuss the key points make the differences for each cavity design. The key point is the separation distance between the InGaAsP gain medium and Si-PC cavity. Figure 2-14(a)-(c) shows the schematic device structure of the PCSEL-I, PCSEL, and PCSEL-III, respectively. From Figure 2-14(a), we find there is a 130 nm cladding layer underneath the InGaAsP MQW for PCSEL-I. For PCSEL-II, on the other hand, the InGaAsP MQW is directly built on the Si-PC without gap. We attribute the higher coupling efficiency mainly to the smaller separation distance between the InGaAsP MQW layer and Si-PC. Please note the confinement factor of Si-PC (Γ_{PC}) is proportioned to the separation distance in the cavity. In the work of PCSEL-III, the separation distance is designed to be 70 nm, including a 30 nm cladding layer and a 40 nm contact layer for future current injection process. One can see that more field distributed in the Si-PC region is indicative of a higher coupling efficiency of 46% for PCSEL-II.

Also, the much improved field confinement in the Si-PC region indicates a much stronger optical feedback in cavity. It is worth to highlight again the principle of the lasing modes in the PCSEL cavities is based on the bandedge modes of 2D PC close to the second order Γ points, where the group velocity of these modes is close to zero. In such 2D PC cavities, the periodic patterned structure is designed close to the unpatented

active region to provide strong in-plane DFB and the standing wave is formed in multidirectional directions due to 2D DFB effect. Simultaneously, the in-plane propagating waves are diffracted toward the vertical direction by the PC structure itself due to the first-order Bragg diffraction. Consequently, the higher coupling efficiency will carry out higher output power diffracted from in-plane. We will verify and analyze the lasing characteristics in the chapter 3.

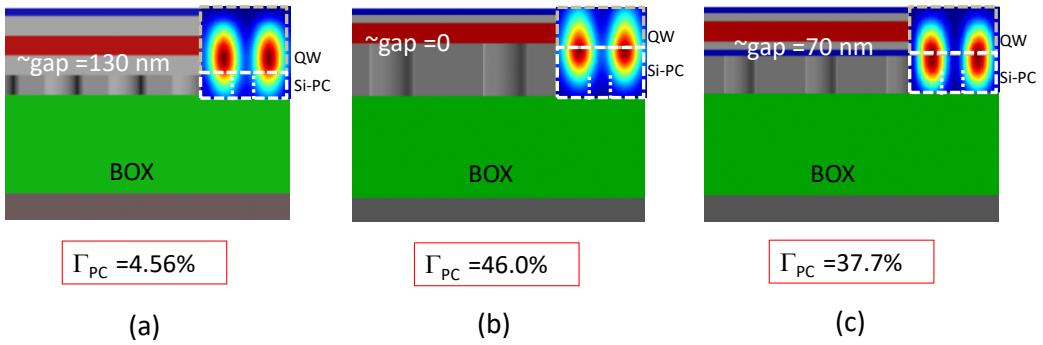

Figure 2-14 Cross section views of schematic of Si-PC bandedge laser cavity structure and field distributions in the xz plane (left) for (a) Mode A in PCSEL-I. (b) Mode C in PCSEL-II. (c) Mode D in PCSEL-III.

2.4 Device Fabrication

A lasing cavity consists of a transferred III-V InGaAsP MQW heterostructure active region, printed on a single-layer Si-PC cavity. A InGaAs/InP sacrificial bilayer was grown first on InP substrate for selective wet-etching and substrate removal. Total thickness of the InGaAsP MQW is 427 nm, 297 nm, and 368 nm for device PCSEL-I, PCSEL-II, and PCSEL-III, respectively. The thickness of the Si-PC was also different according to the designed resonance wavelength range. To integrate the patterned InGaAs membranes on Si-PC, a 2D 1.5 × 1.5 mm^2 square lattice PC pattern was fabricated based on the standard e-beam lithography (EBL) patterning technique and plasma dry-etching processes as shown in Figure 2-15(a). We first define the 4 x 4 square mesas array on MQW heterostructure using photolithography, following with the selective wet etching through the InGaAs/InP sacrificial layer (Figure 2-15 (b)). Substrate removal process is used here for the release of InGaAsP MQW arrays from the native InP substrate with black wax as the protection layer on top (Figure 2-15(c)). The InP substrate was removed by immersing the sample in 20%HCl + 80%H_3PO_4 for about three hours.

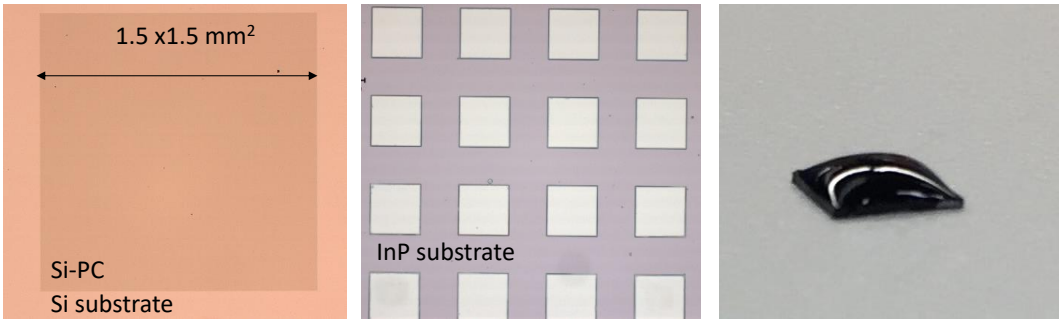

Figure 2-15 (a) A micrograph image of a fabricated Si-PC on an SOI substrate. (b) Micrograph images of 4 x 4 InGaAsP mesa on original InP substrate. (c) A micrograph image of sample covered by Apiezone wax as a protection layer.

The active region was then lifted off as a membrane by selective wet etching to release the bottom InGaAs/InP sacrificial bi-layers. Please note that the InGaAs n-contact layer was removed away based on the cavity design of 25 K operation temperature. For PCSEL-II, both the bottom InP n-cladding and contact layer were selectively etched away to achieve strong coupling efficiency. No any further etch process is required for PCSEL-III. The released InGaAsP MQW membrane is finally printed onto the patterned Si-PC cavity. Wax was removed with trichloroethylene (TCE) and IPA solutions. Figure 2-16 shows the step by step process flows of the PCSEL device fabrication.

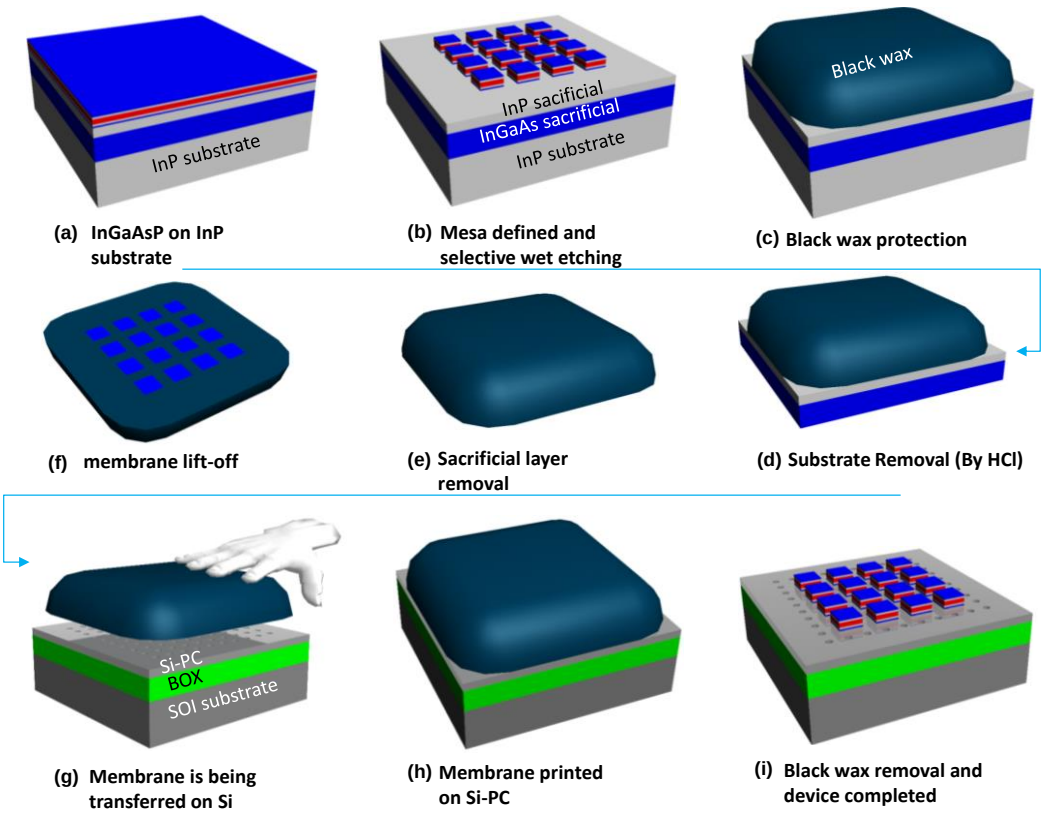

Figure 2-16 Schematic of the steps to fabricate hybrid III-V/Si PCSEL on SOI substrate.

At the end, 4 x 4 arrays with 300 × 300 μm^2 square area InGaAsP MQW is integrated on Si-PC cavity with alignment accuracy around 1–2 μ m. Figure 2-17(a) shows the SEM top view of a printed InGaAsP QW membrane array on a Si PC cavity on a SOI substrate, with a zoomed-in view and a cross-sectional view shown in Figure 2-17(b) and (c), respectively. The measured PL spectra before and after transfer were also plotted together to verify the fabrication quality. It is worth to highlight that this approach enable the most efficient use of III–V materials in lasers without using multiple III–V wafers to cover the entire area of a large silicon wafer, with the additional advantage of recycling the III–V substrates.

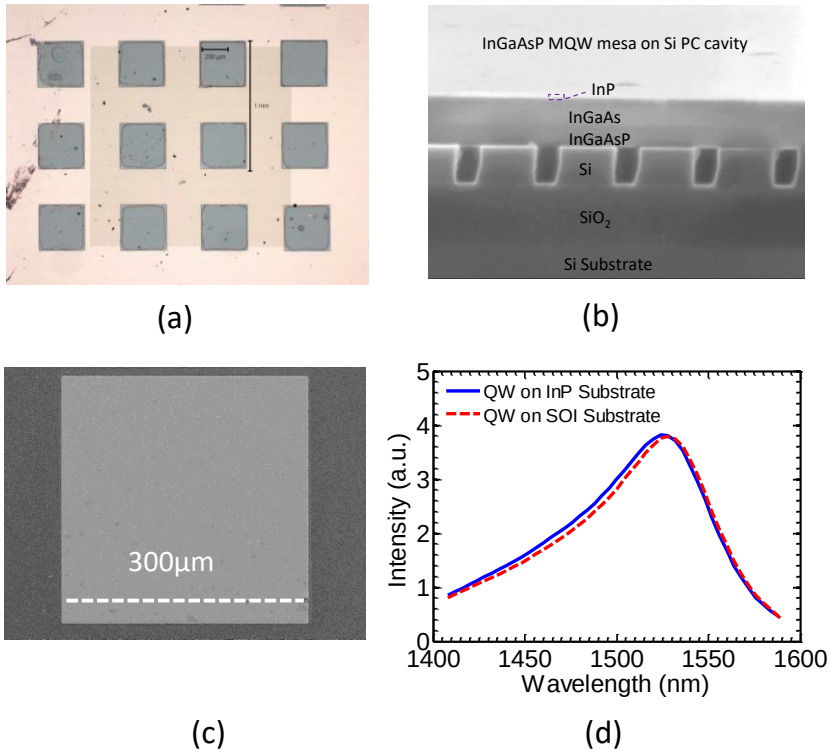

Figure 2-17 (a) Microscope image of 4 x 4 InGaAsP MQW membrane successfully transferred onto Si-PC cavity. (b) SEM cross-view of a InGaAsP MQW membarne transferred onto Si-PC cavity. (c) SEM top view image. (d) Measured PL spectra of the devices before and after transferred.

Chapter 3 Measurement and Lasing Characteristics

3.1 Micro-Photoluminescence Setup

Device characterizations are carried out by mounting the devices inside a cryostat and characterized with a monochrometer-based micro-photoluminescence (μ-PL) set up, as shown in Figure 3-1. A continuous wave (c.w.) green (532 nm) laser is used as the pump source incident from the surface normal direction via a long working distance objective lens (M=10 x). The diameter of the excitation spot is around 110 μm. The emitted light was also collected from the same objective lens and separated with a cold mirror. The collected emission light was sent into the monochrometer and detected with a thermoelectric-cooled InGaAs photodetector. A chopper and lock-in amplifier are used for the spectral acquisition of lasing output. An infrared (IR) camera is mounted at the other output port of the monochrometer to acquire the far field image. A polarizer is placed in front of the entrance of the monochrometer to investigate the polarization properties of the emission beams.

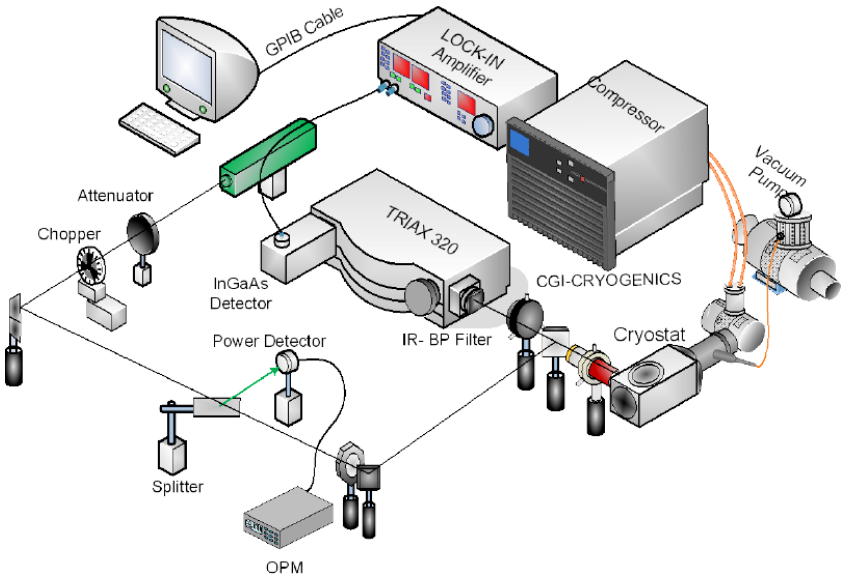

Figure 3-1 Schematic of optically pumped micro-photoluminescence (μPL) setup based on monochromater TRIAX320 spectrograph both for LT and RT measurements and a 300 mW green laser (532 nm) are employed as a pump laser [37].

3.2 Room Temperature PCSEL on SOI

Here we describe the lasing characteristics of the room temperature device PCSEL-III. The optical characteristics of this photonic crystal surface emitting laser (PCSEL) device were measured by a μ-PL setup introduced in previous section. Figure 3-2(a) shows the L-L plot (light output for different input light pump powers) and linewidth as a function of the pump power measured on the surface of the focusing plane. A threshold power density of 0.25 kW/cm^2 was obtained. The measured spectral linewidth was reduced from ~14 nm (below threshold) to 0.54 nm (above threshold). Notice a thermal rollover was observed at optical pumping intensities higher than 0.4 kW/cm^2.

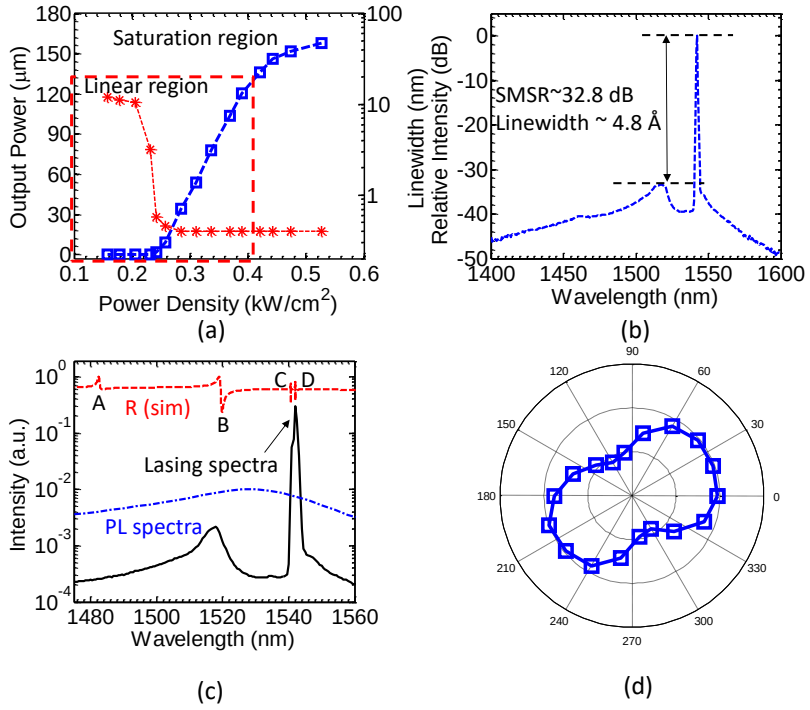

Figure 3-2 (a) Lasing power and linewidth versus input power density at room temperature; (b) Lasing spectral output (plotted in semi-log scale) above the pumping threshold. (c) Simulated reflection spectrum (red-dashed line), the measured laser emission spectrum (solid black line), and the QW PL spectrum (blue-dashed line) for PCSEL-III at room temperature. (d) Measured polarization properties above threshold at λ = 1542 nm.

A spectrum of the laser line above threshold plotted in semilog scale are shown in Figure 3-2(b), the peak wavelength, full width at half-maximum (FWHM) of the spectrum, and side mode suppression ratio (SMSR) are 1542 nm, 0.54 nm, and 31.8 dB, respectively. Figure 3-2(c) show the simulated reflection spectra, measured lasing spectra, and reference PL spectra. These measured lasing modes correlate well with the TE guided modes (modes D) in the reflection spectra for PCSEL-III. Additionally the lasing output shows one slightly polarization, as shown in Figure 3-2(d).

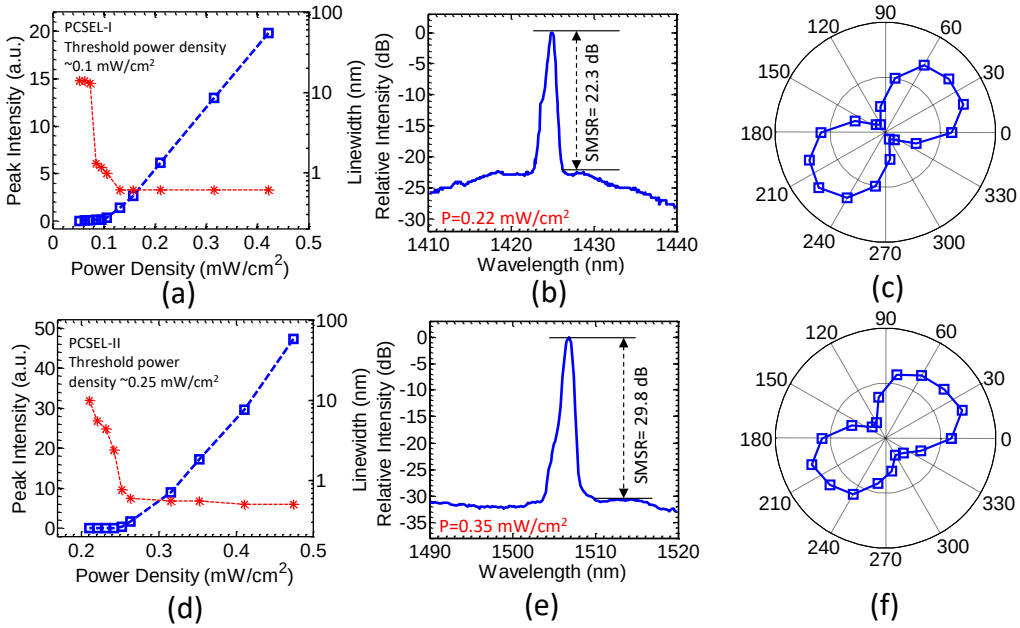

Figure 3-3 (a) Lasing power and linewidth versus input pump power for PCSEL-I at T = 25 K. (b) Lasing spectral output (plotted in semi-log scale) above the pumping threshold for PCSEL-I. (c) Measured polarization properties above threshold at λ = 1424 nm. (d) Lasing power and linewidth versus input pump power for PCSEL-II at T = 180 K. (e) Lasing spectral output (plotted in semi-log scale) above the pumping threshold for PCSEL-II. (f) Measured polarization properties above threshold at λ = 1505 nm.

In addition, The L-L plot and the corresponding spectral linewidths are shown in Figure 3-3(a) for PCSEL-I operating at T = 25 K. The threshold pump power is 0.11 kW/cm^2. The measured spectral linewidths are reduced from ~12 nm (below threshold) to

0.7 nm (above threshold). Shown in Figure 3-3(b) is the measured lasing spectrum above threshold. Single mode lasing was observed at around 1424 nm with a narrow linewidth of 0.7 nm, which is essentially limited by the measurement set-up. The SMSR reaches ~22 dB for the pump power P = 40 mW. Additionally the lasing output shows one dominant polarization, as shown in Figure 3-3(c). The measured results for PCSEL-II designed for the T = 180 K operation are presented in Figure 3-3(d–f). A pumping threshold of 0.25 mW/cm^2 was observed with the linewidths reduced from ~10 nm to 0.6 nm. The measured single mode lasing spectrum is displayed in Figure 3-3(e) where one can see a SMSR of 28 dB at a pumping power of 50 mW. Correspondingly, the output is also polarized.

Figure 3-4(a)-(b) show the simulated reflection spectra (the incident angle θ = 0.2° is used here) and measured lasing spectra for PCSEL-I and -II, respectively. Broadband PL emission spectra are also shown as references at these two different operation temperatures. These measured lasing modes correlate well with the TM guided modes (modes A for PCSEL-I and mode-C for PCSEL-II) in the reflection spectra for these two devices, respectively. The detail numerical information is listed in Table 2-2.

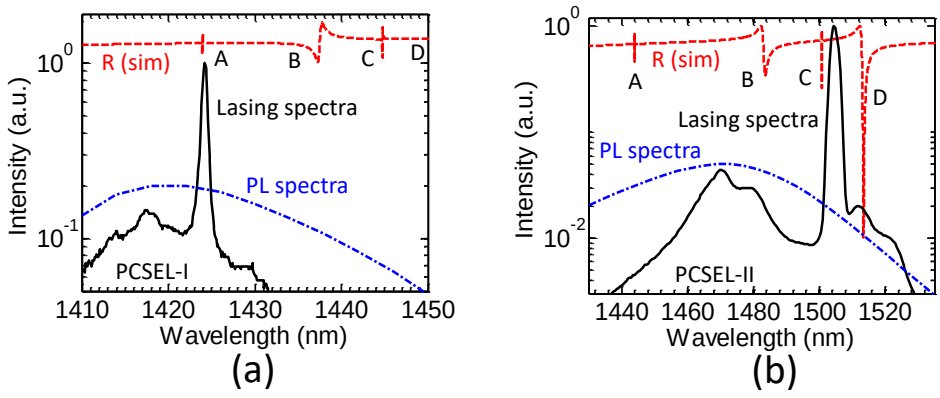

Figure 3-4 (a) Simulated reflection spectrum (red-dashed line), the measured laser emission spectrum (solid black line), and the QW PL spectrum (blue-dashed line) for PCSEL-I at T = 25 K. (b) PCSEL-II at T=180 K.

3.3 Lateral Size Scaling of PCSEL

The PCSEL devices demonstrated so far have relatively large lateral sizes, typically around 100 μm. Such a large in-plane size (L=200a) can be regarded as an infinite structure, so the lateral loss will be very small and can be ignored [42]. However, when the device becomes smaller, the lateral loss will have significant impact on the lasing threshold. Therefore, in this section, we will investigate the lateral dimension influence to the PCSEL devices and propose a few simple ways to reduce the lasing threshold by increasing the lateral confinement.

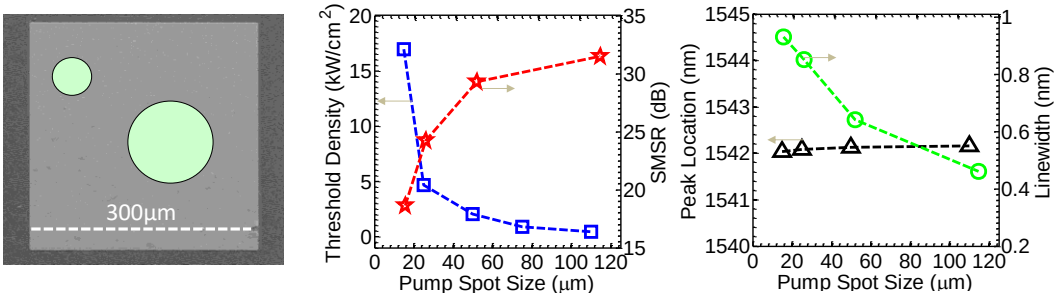

Figure 3-5 (a) Illustration of the pumping spot size and position in the experiment, in which the device size is 300 μm x 300 μm; (c) Lasing threshold and SMSR versus pump spot size; (d) Lasing peak location and linewisth versus pumping spot size.

The room temperature device (PCSEL-III) was used here to verify this concept experimentally. We first varied the optical pumping spot size to investigate the lateral size effect with the weak confinement. Figure 3-5(a) shows the scanning electron microscopy (SEM) image of a room temperature PCSEL on silicon-on-insulator (SOI) and the illustration pumping spot size at different positions during the measurement. The device characterization procedure is the same as the one described in previous section. The initial diameter of the excitation spot is around 110 μm. Another long working distance objective lens (x 50) was added to the measurement system along with the precision pinholes to reduce the spot size of the incident light to 50 μm, 25 μm, and 15 μm,

respectively. Please note the pump energy is normalized to the excitation area for comparison. From Figure 3-5(b), we note that the threshold density increases to around 16.8 kW/cm^2 as the pump spot size reduced to 15 μm, while the SMSR decreases from 31.4 dB to 18.6 dB with decreasing spot size. The lasing linewidth also increases when the pump spot size reduces to 50 μm or smaller (Figure 3-5(c)). However, the emission wavelength remains relatively constant at 1,542 nm. These results indicate that the when the pump spot size is relatively small, the device is excited at a state of weak lateral confinement with low coupling efficiency. Due to the deficiency of coupling, the laser threshold is much higher compared to the sufficient coupling strength. Conversely, when the pump spot is increased to overcome another limit, the device will be excited at a state of strong lateral confinement with over coupling efficiency [43]. Hence, the laser threshold density cannot be further decreased and reaches a saturation value.

The second PCSEL structure we intend to enhanced lateral confinement by introducing strong index different at the device boundary. In the beginning, we transfer and printing a relatively large InGaAsP membrane around 600 x 600 μm^2 on silicon photonic crystal (Si-PC) cavity. The lateral dimension and vertical dimension of the cavity were considered as infinite and zero etching, respectively. The schematic cavity structure is shown in Figure 3-6(a). Next, we fabricated two sets of devices: the first set of devices is partially etched down to 300 nm (only etched quantum (QW) well layer), where the schematic cavity structure is shown in Figure 3-6(b). The cavity dimension in this case was considered as the QW membrane size as same as previous structure. The second set of devices is completely etched down to box (520 nm as shown in Figure 3-6(c). In the case, Si-PC and QW mesa have the same in-plane size. Due the larger index contrast between the InP/Si and air, the interface will provide larger in-plane reflection. So the cavity in-plane loss will reduce and the total *Q* factor can increase, i.e. the gain

threshold will be reduced. Furthermore, each set of device have different dives size of 20 μm, 50 μm, 75 μm, and 100 μm. The photo images of these two fabricated derives are shown in Figure 3-6(a) and (b), respectively.

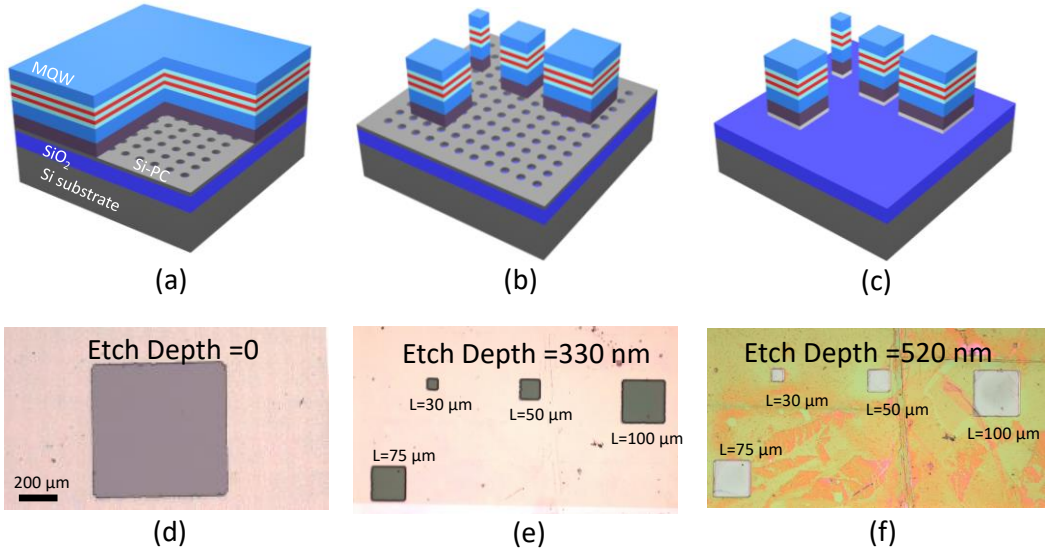

Figure 3-6 (a) Schematic of PCSEL with zero etching depth. (b) Schematic of PCSEL with 330 nm etching depth. (c) Schematic of PCSEL with 520 nm etching depth. (d) Photo image of 600 x 600 μm^2 PCSEL on Si PC cavity. (e) Photo image of PCSELs with different size at 330 nm vertical etching depth. (f) Photo image of PCSELs with different size at 520 nm vertical etching depth.

The measured lasing threshold density versus device size was shown in Figure 3-7(a). We note that the lasing threshold density increases with decreasing device size in three cavity schemes. Additional, the threshold density shows an inverse relationship with vertical etch depth. The SMSR, in contrast, shows a quite different behavior as shown in Figure 3-7(b). The SMSR decreases with decreasing device size. This behavior can be understood as follows. For small device size, the major loss mechanism in the laser is the in-plane loss. In particular, at very short cavity dimension, the high threshold density was mainly due to the energy leakage through gain region at the boundary of the laser cavity. However, in deeper vertical etching cavity scheme, large refractive index difference

between Si-PC and air at cavity boundary provides sufficient coupling feedback and enhanced lateral confinement. For a relatively small device size, e.g. L <50 μm, the influence of the in-plane loss on threshold behavior is drastically increasing, leading to the extreme high threshold density and low SMSR in lasing characteristics.

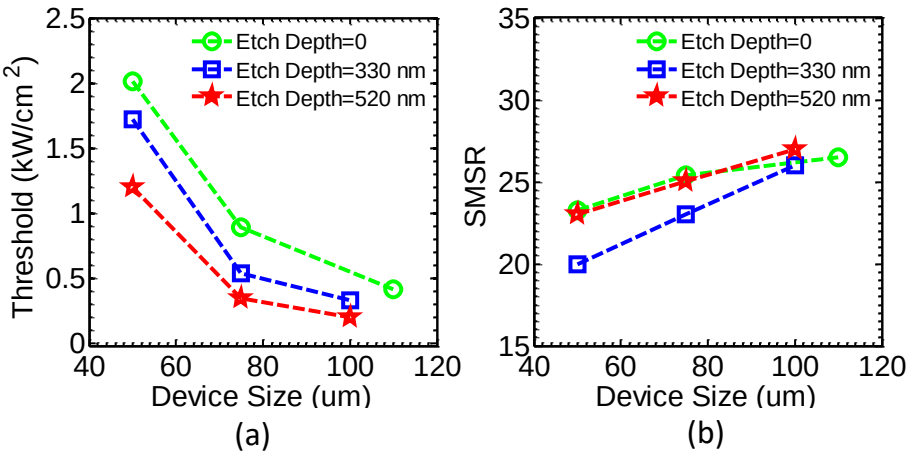

Figure 3-7 (a) The measured lasing threshold of three cavity schemes versus device size. (b) The measured SMSR of three cavity schemes versus device size.

To clarify the lasing characteristics dependent on cavity lateral dimension accurately. We also performed the simulations to investigate the gain threshold and quality factor (*Q*) behavior versus the device size. The simulations are first employed by using the Fourier Modal Method with Stanford Stratified Structure Solver (S_4) software package [38]. Next, we calculated the gain threshold and *Q* factors from lasing cavity mode in simulated spectrum. Initially, the device size is considered over 100 μm, which can be regarded as infinity. By varying the dimension in the simulation, the corresponding gain threshold was estimated according to the equation below:

$$g_{th} = \frac{\alpha}{\Gamma_{QW}} = \frac{2\pi}{Q \bullet a} \times \frac{1}{\Gamma_{QW}} \tag{6}$$

The *Q* factors are obtained by Fano fitting the guided resonances in reflection spectra [44], where the Γ_{QW} can be extracted from equation (2) and (3) based on previous discussion. Figure 3-8(a) displays the calculated gain threshold and *Q* factor plotted versus device size. We can see the gain threshold increases rapidly as device size decrease from 80 μm to 20 μm. On the other hand, the *Q* factor shows the reverse trend as device size decrease. This simulation results agree well with the lasing characteristics dependent on cavity dimension, which point out that the influence of the in-plane loss has to be taken into account in finite device size. In other words, the relatively less periodicity of the Si PC contributes to deficient in-plane coupling efficiency. As the result, the power is escaping from the edges of the laser cavity due to the weak lateral confinement.

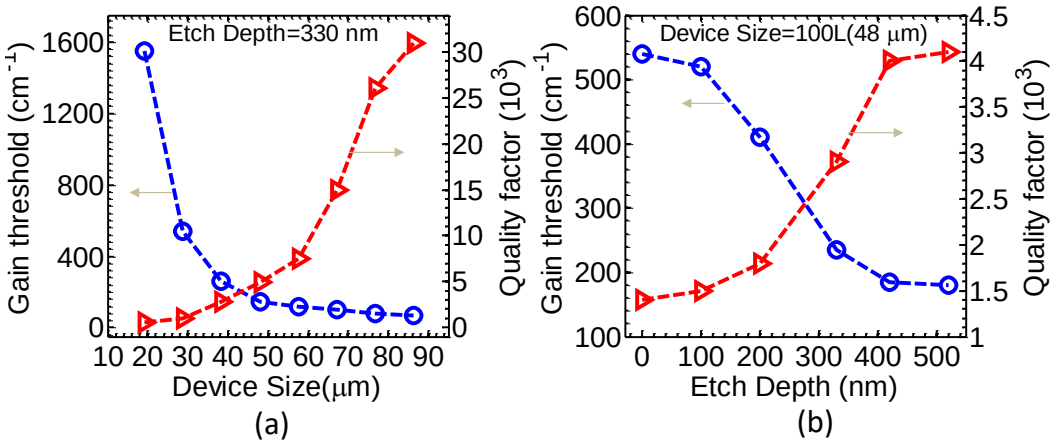

Figure 3-8 (a) The simulated gain threshold and *Q* factor versus the different device size. (b) The simulated gain threshold and *Q* factor versus the different etching depth.

By controlling the vertical etch depth, we are able to increase the lateral confinement due to large index contrast in the device boundary. To confirm this concept, the simulation is carried out based on same device parameters mentioned above. The device size is fixed at 50 μm and the vertical etching depth is considered as a variable parameter in this case. Figure 3-8(b) shows the gain threshold and *Q* factors change

versus vertical etching depth, where we can see the gain threshold decrease drastically from 500 cm^{-1} to 200 cm^{-1} when the etching is deeper. On the other hand, the *Q* factors increase quickly from 1,500 to 4,000, especially in the etching range of 200-400 nm. We attribute this to the much higher lateral confinement (compared to previous works) realized due to high reflection in the device boundary of MQW/Si-PC and air. The large refractive index difference is an indicator of strong in-plane optical coupling, which provides sufficient feedback effects to keep lasing characteristics even though the device size is shrinking.

From the above simulation and experimental results, we can see the lasing characteristics significantly changed dependent on different in-plane and vertical dimension in PCSEL. The stronger lateral confinement attribute to large index contrast of deep vertical etching scheme at the cavity boundary. This scheme suggests a promising approach to realize the relatively small PCSEL device by trapping more energy inside the cavity. In this work, the numerical analysis of the energy distribution and mode resonance behavior were investigated for each cavity scheme discussed earlier. We also proposed various cavity schemes with supplementary lateral distributed Bragg reflector (DBR) and bottom gold (Au) reflector structures to enhance the cavity confinement. A freely available finite-difference time-domain (FDTD) implementation was used to evaluate the resonance location and cavity *Q* factor [45].

Figure 3-9(a)-(c) show the devices with vertical etched depth in 0 nm, 330nm, and 520 nm, respectively, which are the same structure described in Figure 3-6. The *Q* factor is increasing with the deeper etch depth due to the large index contrast. Furthermore, with introducing the lateral DBR structure adjacent to the active region as shown in Figure 3-9(d), the cavity *Q* factor can be increased to 5,361 by tuning the separation between QW and DBR. Here the separation distance f=600 nm was designed

to achieve extra feedback from the cavity edge to reduce the in-plane loss. Moreover, a huge increase of *Q* factor ~2.5 x 10^6 occurs when a bottom gold (Au) reflector was added in between SiO_2 and Si substrate as shown in Figure 3-9(e). This extreme *Q* factor attribute to the strong in-plane feedback from cavity edge and constructively interference in the vertical direction. In summary, the lateral size has a significant impact on the device lasing performance. When the device becomes smaller, the loss increase and the threshold will increase. We investigated several simple and effective ways to improve the cavity *Q* factor and cavity confinement capability, and demonstrated these concepts in the experiments. All the results here give us the guidance and confidence to achieve smaller PCSEL devices with better performances.

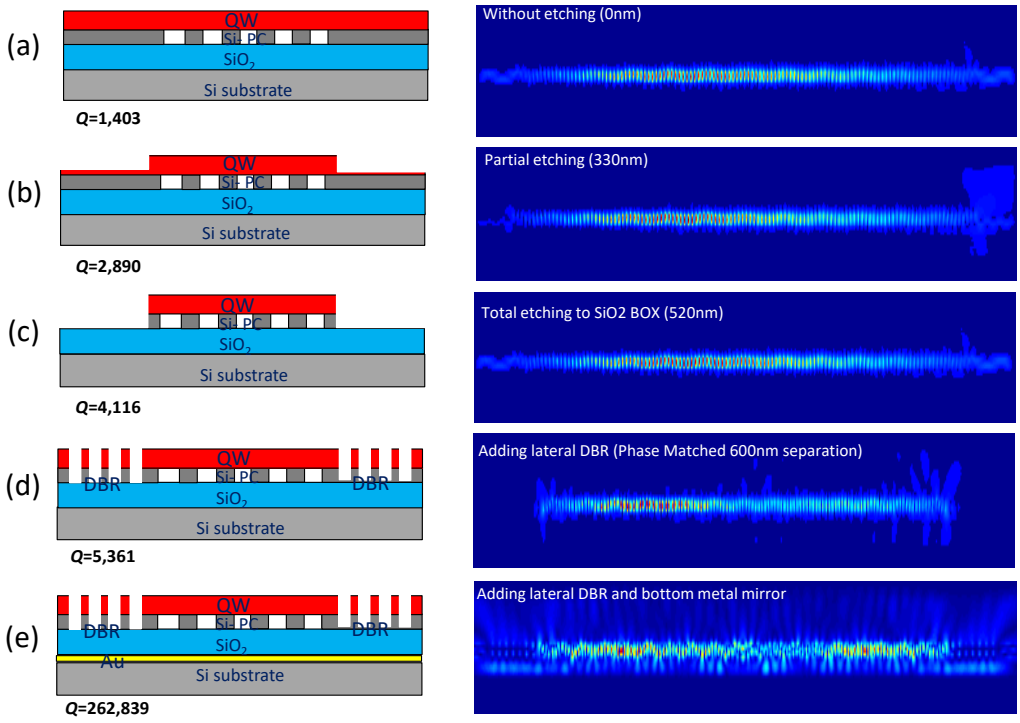

Figure 3-9 Schematics and simulated field distributions of PCSEL cavity with enhanced lateral and vertical confinements.

3.4 Thermal Performance of PCSEL

3.4.1 PCSEL on Bulk Si

Despite the experimental advances that have recently been integrated with the Si substrate, most III-V/Si hybrid lasers reported so far were demonstrated on SOI substrates. The use of SOI substrates still presents a substrate incompatibility issue with conventional Si electronic chips, largely built directly on bulk Si substrates. Additionally, the presence of a low-index buried oxide (BOX) layer underneath the functional Si layer also limits the thermal performance of the photonic devices built on it, especially, lasers, due to the relatively low thermal conductivity of oxide. Thus, it is of great importance to introduce the PCSEL directly built on bulk Si substrate [46-48]. Moreover, thermal simulations showed that lasers integrated with bulk Si substrates demonstrate low thermal resistance, which facilitates high lasing efficiency and high temperature operation [49]. In this section, we first introduced the design and demonstration of the PCSEL directly built on bulk Si. Next, thermal performance was also investigated to realize efficient heat dissipation and low thermal resistance afforded by the architecture of PCSEL on bulk Si substrate.

The Si-PC structure is used as the bottom cladding layer, and the MQW membrane can be printed directly on bulk Si substrate without a low-index oxide buffer layer. The design parameters were carefully chosen for the bottom Si-PC in order to obtain relatively small refractive index. A schematic of a successful design of this structure is shown in Figure 3-10(a), which consists of a transferred InGaAsP MQW membrane on a Si-PC cavity on a bulk Si substrate. Figure 3-10(b) shows the refractive index versus vertical position in the cavity. The cavity was cladded by top air region and bottom Si-PC low refractive index layers to obtain sufficient confinement factor. Figure 3-10(c) shows the refractive index for each layer in the Si-PC cavity. A bulk Si wafer with

550 μm thickness was used here. The 2D square lattice PC pattern on bulk Si substrate was made following the same EBL patterning and dry etching processes.

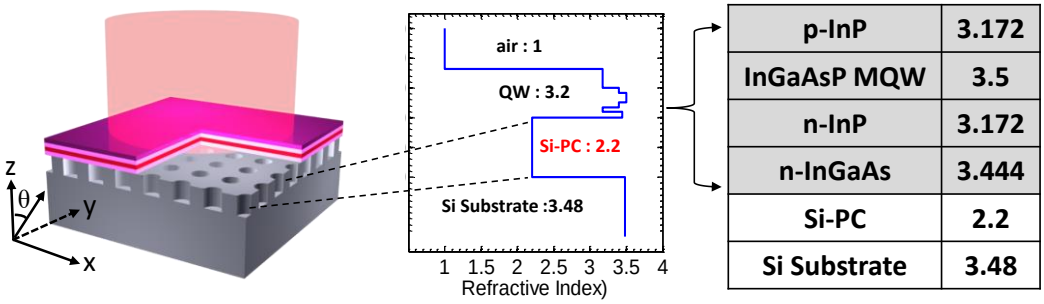

Figure 3-10 (a) Schematic of PC bandedge membrane laser on bulk Si substrate. (b) Cavity refractive index profile. (c) Cavity design structure of laser on bulk substrate.

The SEM top view of Si-PC cavity is shown in Figure 3-11(a). The lattice constant (*a*), air hole radius (*r*), and etched depth (*t*) of the fabricated PC are 540 nm, 243 nm, and 400 nm, respectively. Different from the PCSEL on SOI substrate, the PC structure here was considered as the low refractive index cladding layer of the cavity. The approximate refractive index n_{eff} of the InGaAsP MQW active layer and Si-PC was around 3.5 and 2.2 based on the average dielectric constant in the design. Please note the large air hole radius was required to achieve low refractive index contrast in Si-PC slab. Moreover, the thickness of the Si-PC slab was chosen to be 400 nm to obtain high Q value by reducing the vertical radiation loss. Figure 3-11(b) shows the cross-sectional view of a transferred InGaAsP QW membrane on Si-PC laser cavity on bulk Si substrate. The field profile of the lasing mode is displayed in Figure 3-11(c), where the integrated H-field intensity of the whole cavity along the z-axis direction is plotted together with the cavity index profile.

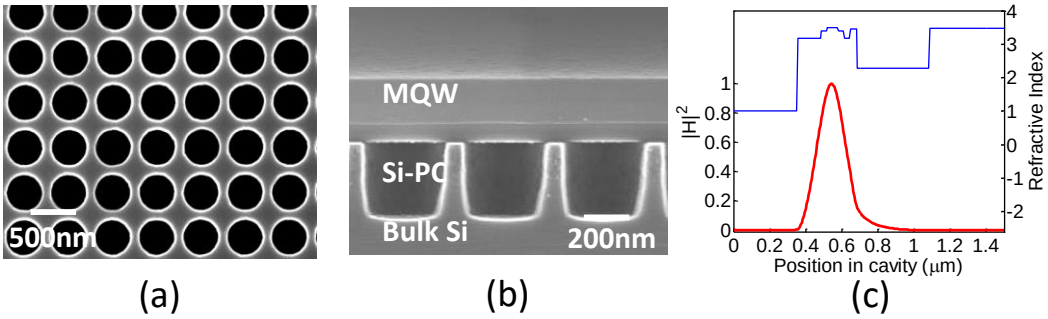

Figure 3-11 (a) Zoomed-in SEM top view of the defect-free Si-PC cavity on bulk Si substrate. (b) Cross-sectional view of a InGaAsP membrane integrated with Si-PC on bulk Si substrate. (c) Field distribution of cavity mode.

To evaluate the laser performance experimentally, the PC bandedge membrane laser on bulk Si substrate was used the same measurement setup outlined in Figure 3-1. Figure 3-12(a) shows the light output and linewidth versus the pump power measured on the surface of the PCSEL on bulk Si substrate. The laser threshold pump power density of 0.4 kW/cm^2 was obtained, where it was around a factor of 2 greater than PCSEL on SOI substrate at similar operation temperatures [39]. We attribute this to the much lower optical confinement factor and less *Q* factor within the cavity due to a larger air hole radius. Figure 3-12(b) presents the measured lasing spectrum above the threshold. The single-mode lasing peak wavelength and linewidth are 1,452 nm and 0.87 nm in the 160 K operation temperature.

Figure 3-12(c) shows the simulated reflection spectra, measured lasing spectra, and reference PL spectra. These measured lasing modes correlate well with the TM guided modes (modes A) in the reflection spectra for PCSEL-III. The calculated *Q* factor is 3.27 × 10^3, which is 2 orders lower than the Q for PCSEL on SOI. However, there are few strategies to improve the laser characteristics of present cavity design on bulk Si substrate, such as the introduction of vertical asymmetry in the air-hole structure and

effective utilization of tailoring the vertical etched profile. The *Q* factor can be theoretically increased much higher above 3,000, which would achieve lower threshold pump power density in the 160 K operation temperature. Additionally the lasing output shows one slightly polarization, as shown in Figure 3-12(d).

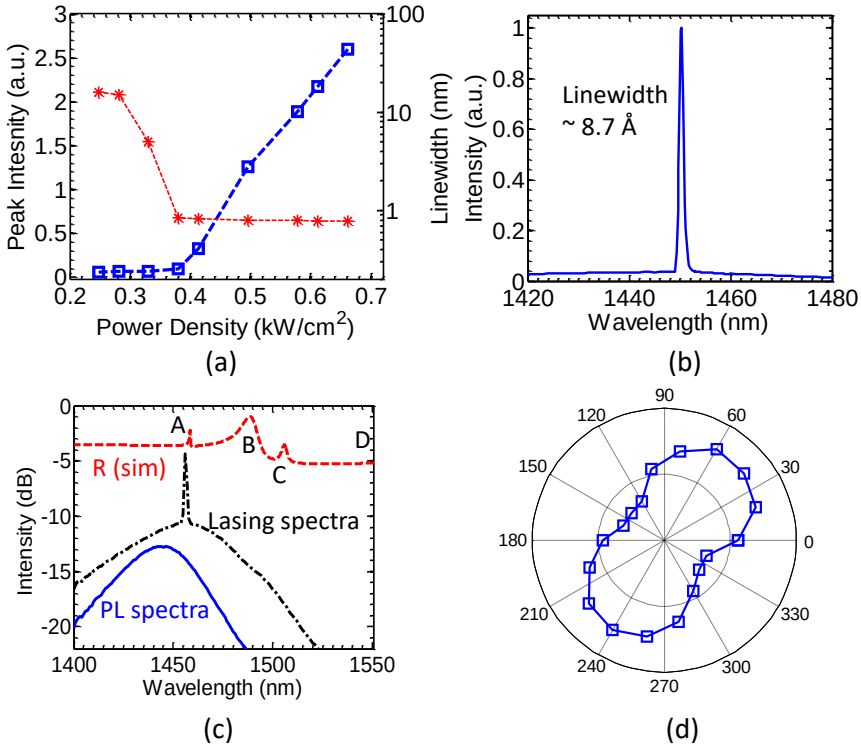

Figure 3-12 (a) Lasing power and linewidth versus input power density at T=160 K for PCSEL on bulk Si substrate. (b) Emission spectrum of the laser above threshold. (c) Simulated reflection spectrum (red-dashed line), the measured laser emission spectrum (solid black line), and the QW PL spectrum (blue-dashed line) for PCSEL on bulk Si at T=160 K. (d) Measured polarization properties above threshold at λ = 1452 nm.

3.4.2 Thermal Resistance

In order to compare the thermal performance, here we prepared two PCSELs built onto bulk Si substrate and SOI substrate, respectively. The laser cavity for both devices is designed to operate at similar temperatures and emission wavelengths. The thicknesses of each layer of the InGaAsP MQW membrane and the parameter of Si-PC are listed in Table 3-1.

Table 3-1 Cavity Design Structure of Laser on Bulk Si and SOI

Layer materials	**Laser on Bulk Si**	**Laser on SOI**
***p*-InP**	**130 nm**	
InGaAsP MQW	**127 nm**	
***n*-InP**	**130 nm**	
***n*-InGaAs**	**40 nm**	
Si-PC	**400 nm, *a*=540 nm *r/a*=0.45**	**190 nm, *a*=480 nm *r/a*=0.15**
SiO2	**0**	**400 nm**
Si substrate	**525 μm**	

The bulk Si substrate is expected to dissipate more heat along the vertical direction from the surface of the cavity to the bottom substrate and heat sink. A figure of merit to quantify the heat dissipation out of the cavity is the thermal resistance [50, 51]. By extracting the shift of emission peak wavelength with varying the temperature and pump power, the thermal resistance of the laser can be mathematically defined by the following ratio:

$$R_{th} = \frac{\frac{\Delta\lambda}{\Delta P_{heat}}|T = const.}{\frac{\Delta\lambda}{\Delta T}|P = const.} \sim \frac{\frac{\Delta\lambda}{\Delta P_p}|T = const.}{\frac{\Delta\lambda}{\Delta T}|P = const.} \quad (7)$$

Here, the ΔP_{heat} is the heat generated from the cavity and ΔP_p is the total pump power. We assume heat generation is primarily in the QW section [52], and it is linearly proportional to the optical pump power for the operation window between threshold and roll-over. We first characterize the PCSEL on bulk Si substrate. The wavelength spectrum dependence of the pumping power from the PCSEL on bulk Si substrate was measured as shown in Figure 3-13(a). The peak of the emission wavelength slightly shifted towards longer wavelengths when the pump power increased from 25 mW to 50 mW at 160 K. In our measurement, the spectral shift vs power ratio presents the spectral shift vs power generated from the QW region. Secondly, the spectral dependence of the operation temperature varying from 120 K to 200 K at a constant incident power was also measured and shown in Figure 3-13(b). Please note the cavity design of the PCSEL on bulk Si substrate was optimized for device operation around 160 K. Single mode lasing operation was obtained at the 120 K to 200 K range for the pump power at 40 mW. The wavelength shift versus pumping power is calculated to be 0.0125 nm/mW, and the shift versus temperature was 0.0412 nm/K.

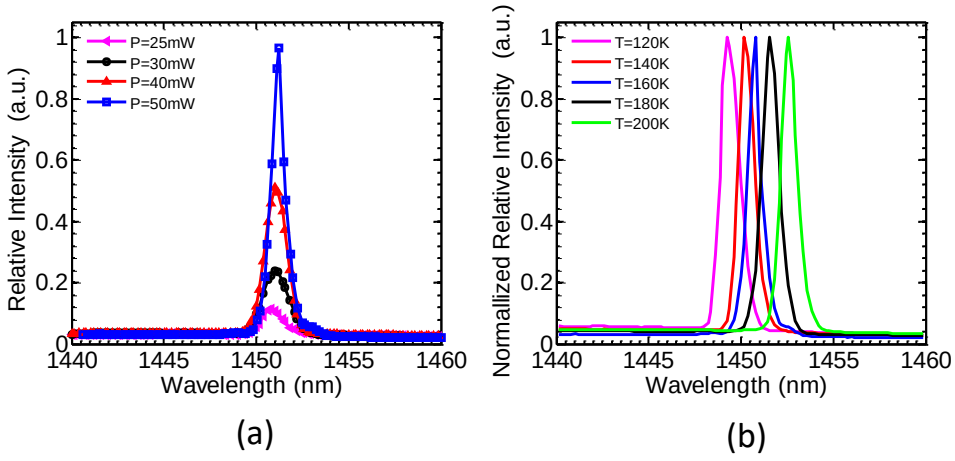

Figure 3-13 (a) Lasing spectra at different pump powers above threshold at constant 160 K. (b) Lasing spectra at different operation temperatures with constant 40 mW pump power.

Figure 3-14(a) and (b) show the measured emission wavelength peak shift at different pump powers and varying operation temperatures for both PCSELs on bulk Si substrate and on SOI substrate operation at 160-180 K. For the PCSEL on bulk Si substrate, the thermal resistance was extracted from Figure 3-14(a) and (b) and calculated to be 303.4 K/W. On the other hand, the thermal resistance of PCSEL on SOI was calculated to be 558.5 K/W. The thermal resistance of PCSEL on bulk Si substrate is therefore around a factor of 2 times lower than that of a structure with a BOX layer. We attributed the higher thermal resistance to the low thermal conductivity of the BOX layer. It is also worth noting that the thermal resistance values calculated here is a relative value, as the absolute value should be based on the exact heat source (ΔP_{heat}), which is not known here.

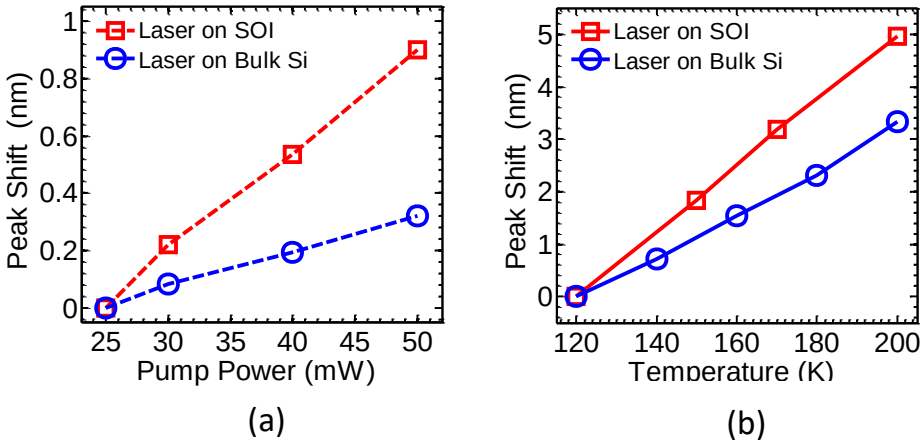

Figure 3-14 (a) Emission peak wavelength shift versus pump powers for PCSEL on SOI and on bulk Si substrate. (b) Emission peak wavelength shift versus operation temperatures for PCSEL on SOI and on bulk Si substrate.

To better understand the heat dissipation related to thermal resistance, thermal simulation was carried out using ANSYS [53]. Figure 3-15(a) and (b) show the device structure used in the thermal simulation for PCSEL on SOI substrate and bulk Si

substrate, respectively. The simulated temperature rise (ΔT) distributions inside the PCSEL on SOI substrate and on bulk Si substrate are shown in the Figure 3-15(c) and 27(d), respectively. The top layer represents the MQW region which has been assumed to be the main heat source in the simulation. The bulk Si substrate dissipates more heat along the vertical direction from surface of cavity to the bottom substrate, which promises the excellent cooling management.

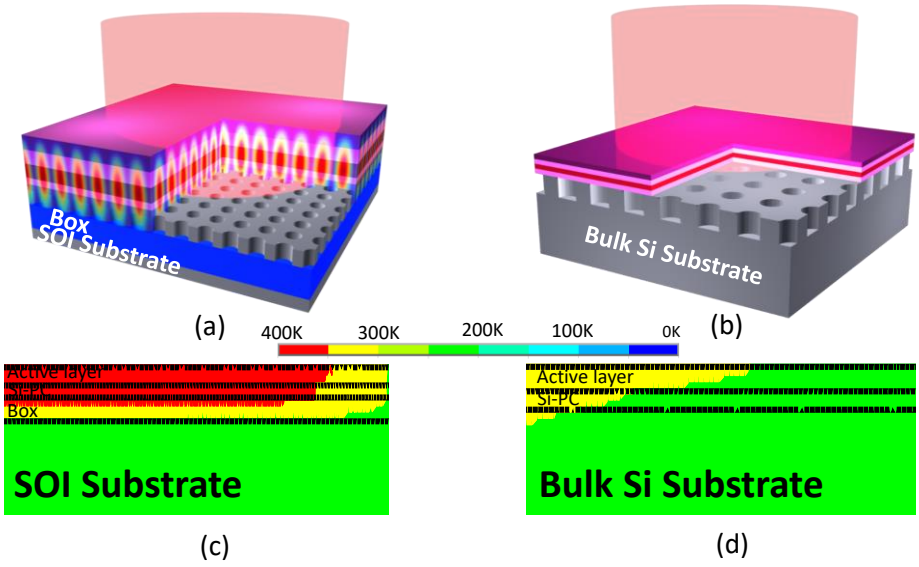

Figure 3-15 (a) Schematic of the PCSEL on SOI substrate. (b) Schematic of the PCSEL on bulk Si substrate. (c) Thermal field distributions of PCSEL on SOI substrate with 400 nm BOX. (d) Thermal field distributions of PCSEL on bulk Si substrat.

3.5 Discussions

We successfully demonstrated a hybrid III-V/Si PCSEL, based on a transferred InGaAsP MQW structure on Si substrate. With the careful cavity design, single mode lasing under room temperature optical pumping was achieved with a linewidth ~5.4 Å and a SMSR of 31.8 dB. In our experiment, the finite-size effects were also investigated to understand the importance of laser output characterizations. The different behaviors of emission wavelength, lasing linewidths, SMSR, and threshold power density are summarized by adjusting the incident pump spot size and the cavity dimensions. We also propose the strategies to mitigate the lateral loss by incorporating supplementary in-plane and vertical confinement schemes.

Another important cavity design of the PCSEL directly built on bulk Si substrate was also reported. The excellent heat dissipation from the active region and minimized temperature rise of the lasing cavity was also demonstrated experimentally, and agree well with the simulation. Finally, the experiment results were also correlated to theoretical and numerical analysis to understand the mode properties and thermal performance.

Chapter 4 Electrically Pumped PCSEL

4.1 Buried Tunneling Junction and Cavity Design

In the current injection point of view, a multi-quantum well (MQW) active region is disposed between the *n*-type (electron carrier) and *p*-type layers (hole carrier), allowing the electrons to recombine with the holes and thus emit photons. In several respects, *p*-type material is more difficult to work with than n-type material and tends to be operationally inferior with regard to carrier mobility and overall electrical efficiency. Also, in vertical surface emitting scheme, the *p*-type material absorbs the emitted photons, reducing the laser output. Therefore, minimizing the volume of the *p*-type material is desirable. In addition, the injection issue, i.e. non-uniform current injection, current crowding, and sidewall leakage current, are the major challenges in the development of such large and thin membrane photonic crystal surface emitting laser (PCSEL). To address these issues, the applied buried tunneling junction (BTJ) shows promising approach to suppress the current spreading and enabled the laser radiation confinement without any mesa formation at the same time. This technology involves burying a highly *n*++ doping tunnel junction adjacent to the p-type cladding layer, which converts the top contact layer into n-type material. Thus, reduced heat generation in the devices is expected [54, 55]. Recently, BTJ has been employed for long-wavelength membrane light source, which presented several of features, such as highly strained active region [56], highly doping levels for reduced intrinsic parasitic [57], and high speed application [58].

In this section, we report the design and demonstration of electrically pumped PCSEL on silicon (Si) substrate by employing BTJ structure as a current spreading control. The detail design of BTJ quantum well (QW) structures, silicon photonic crystal

(Si-PC) cavity, and mask layout were introduced, followed by the process flows and lasing characteristics.

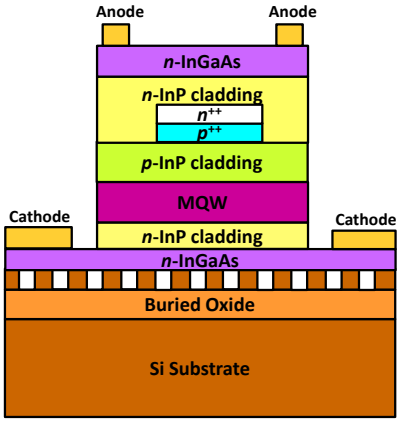

(a)

Description	Materials	BTJ-PCSEL
Contact layer: n	InGaAs	40 nm
Cladding layer: n	InP	80 nm
BTJ: n^{++}	InGaAs	20 nm
BTJ: p^{++}	InAlGaAs	10 nm
Cladding layer: p	InP	265 nm
MQW	InGaAsP	127 nm
Cladding layer: n	InP	31.5 nm
Contact layer: n	InGaAs	40 nm
Photonic crystal	air hole Si-PC	125nm, r/a=0.15
BOX	SiO2	400nm
Substrate	Si substrate	525µm

(b)

Figure 4-1 (a) Schematic of a electrically pumped BTJ PCSEL on Si substrate. (b) Key design parameters of InGaAsP QW cavity with embedded BTJ region on SOI substrate.

The schematic cross-section view of the electrically pumping BTJ PCSEL on Si substrate is shown in Figure 4-1(a). Here we design the cavity structure operated at room temperature. The lasing cavity consists of a transferred III-V InGaAsP MQW heterostructure with embedded BTJ region, printed on a single-layer Si-PC cavity. The total thicknesses of the InGaAsP MQW heterostructure with embedded BTJ and parameters of Si-PC are listed in Figure 4-1(b). The corresponding Si-PC cavity was designed based on a silicon-on-insulator (SOI) substrate, and fabricated using electron beam lithography (EBL) and chemistry reactive ion etching (RIE). The lattice constant *a* of the cavity is designed to be 480 nm according to second `Bragg diffraction condition to achieve the emission wavelength close to 1,550 nm, same as the optically pumped device (PCSEL-III). Additional, the air hole radius and slab thickness are designed to be $r = 0.15a$ and t =125 nm, respectively.

Figure 4-2 shows a schematic of the BTJ QW growth process steps. In first step, the InGaAsP QW was grown on (001) *n*-InP substrate by metal organic chemical vapor deposition (MOCVD), which consists of eight strain-compensated InGaAsP QWs, sandwiched in between top InP cladding layer, bottom InP cladding layer, and bottom InGaAs contact layer as shown in Figure 4-2(a). The highly doped 10 nm p^{++} InGaAsAl and 20 nm n^{++} InGaAs layer were then grown sequentially. In second step, the as- grown wafer was wet etched to form a ridge of BTJ mesa as shown in Figure 4-2(b). Please note the BTJ mesa is defined by etching through the 20 nm n^{++} InGaAsAl and 10 nm p^{++} InGaAs layer to *p*-InP cladding layer. Finally, the wafer was sent back for MOCVD to regrow the *n*-type InP cladding layer and n-type InGaAs contact layer as shown in Figure 4-2(c). Detail thickness and doping concentration were descried in Table 4-1.

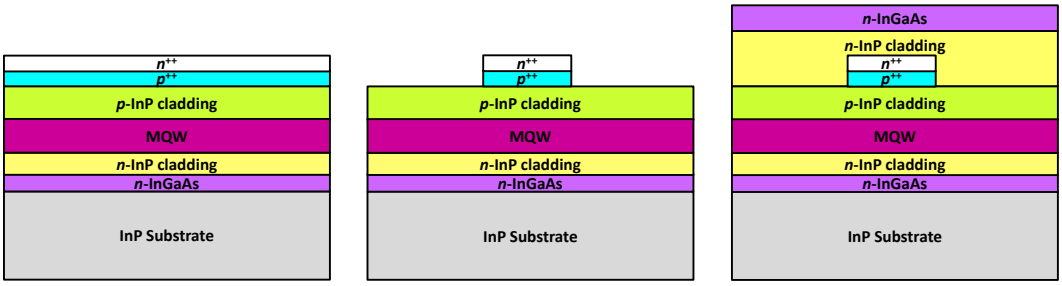

Figure 4-2 Schematic view of a BTJ PCSEL (a) 1st growth (b) BTJ region definition (c) 2nd regrowth.

Table 4-1 Cavity Design Structure of electrically pumped BTJ PCSEL on Si substrate

Layer	Description	Material	Thickness (nm)	Dopant	Doping (cm^{-3})	Optical Index	Optical Thickness
20	Contact layer	InGaAs	40	Si	1e19	3.444	0.0889
19	Cladding layer	InP	80	Si	2e18	3.172	0.163716
<BTJ mesa etching and regrowth>							
18	BTJ: n++	InGaAs	20	Si	5e19-1e20	3.444	0.04444
17	BTJ: p++	InAlGaAs	10	C	5e19-1e20	3.444	0.02222
16	Cladding layer	InP	70	Zn	2e18	3.172	0.040929
15	Spacer layer	InP	195	Undoped (UID)		3.172	0.40929
14	Barrier (0.9% ts)	$In_{0.485}Ga_{0.515}As_{0.83}P_{0.17}$	7.5	Undoped (UID)		3.4	0.0165
5…13	Quantum wells (1% cs) (x8)	$In_{0.76}Ga_{0.24}As_{0.83}P_{0.17}$	7.5	Undoped (UID)		3.5	0.1355
4…12	Barrier (0.9% ts) (x5)	$In_{0.485}Ga_{0.515}As_{0.83}P_{0.17}$	7.5	Undoped (UID)		3.4	0.1316
3	Spacer layer	InP	21.5	Undoped (UID)		3.172	0.044
2	Cladding layer	InP	10	Si	2e18	3.172	0.0205
1	Contact layer	InGaAs	40	Si	1e19	3.444	0.0889
InP Substrate (n+)							

4.2 Electrically Pumped BTJ PCSEL

4.2.1 Fabrication Process

Electrically pumped BTJ-PCSEL on Si was fabricated based on the heterogeneous integration. The lasing cavity consists of a transferred III-V InGaAsP MQW heterostructure active region, printed on a single-layer Si-PC cavity.

The high quality patterned Si-PC cavity was first fabricated via EBL and RIE process on SOI substrates, with 120 nm Si template layer and 400 nm buried oxide (BOX) SiO_2 layer. The two-dimensional (2D) 1.5 × 1.5 mm^2 square lattices Si-PC pattern was made on a 2 x 2 cm^2 SOI die sample. Next, a 6 x 6 mm^2 BTJ InGaAsP QW die sample was prepared and cleaned with acetone and isopropanol. Substrate removal process is used here for the release of top large area InGaAsP MQW membrane from the native InP substrate. Before substrate removal, the surface of BTJ InGaAsP QW die sample is covered by Apiezone wax (mixture of Aapiezone wax and TCE) as a protection layer and left in the air at least 24 hours or waiting until wax harden enough for handle. The InP substrate was etched using mixture solution of hydrochloric acid (HCl) and phosphoric acid (H_3PO_4) with magnetic stirring hotplate at 50 rpm under 4.3 nm/sec etching rate.

After finishing substrate removal, putting one drop of deionized (DI) water on top of prepared Si-PC, placing sample (BTJ InGaAsP QW) and adjusting the position of sample to match with an area of prepared Si-PC. If satisfied with the position of sample, at this point you have to remove an excess of DI water with small wipe paper by gently absorbing it. Typically, sample must be left under pressure p=0.2 N/mm^2 using metal weight and cleanroom wiper placing on top of sample for more than 4 hours to achieve good Van der Waals bonding between QWs and prepared Si-PC surface. To improve the bonding quality, a 30 mins annealing at 150^o process was utilized to enhance the surface

energy of the bonding. Gently removing metal weight and cleanroom swap, and slowly cleaning Apiezone wax with Trichloroethylene (TCE). After wax is cleaned completely, O_2 plasma treatment (RIE power=100 watts; pressure=100 mtorr; gas O2=100 sccm; time=30 sec) is employed to remove residue of remaining TCE from the sample. After transferring the large size BTJ InGaAsP MQW membrane on Si-PC cavity on SOI substrate, the following process is depicted schematically in Figure 4-3(a)–(f).

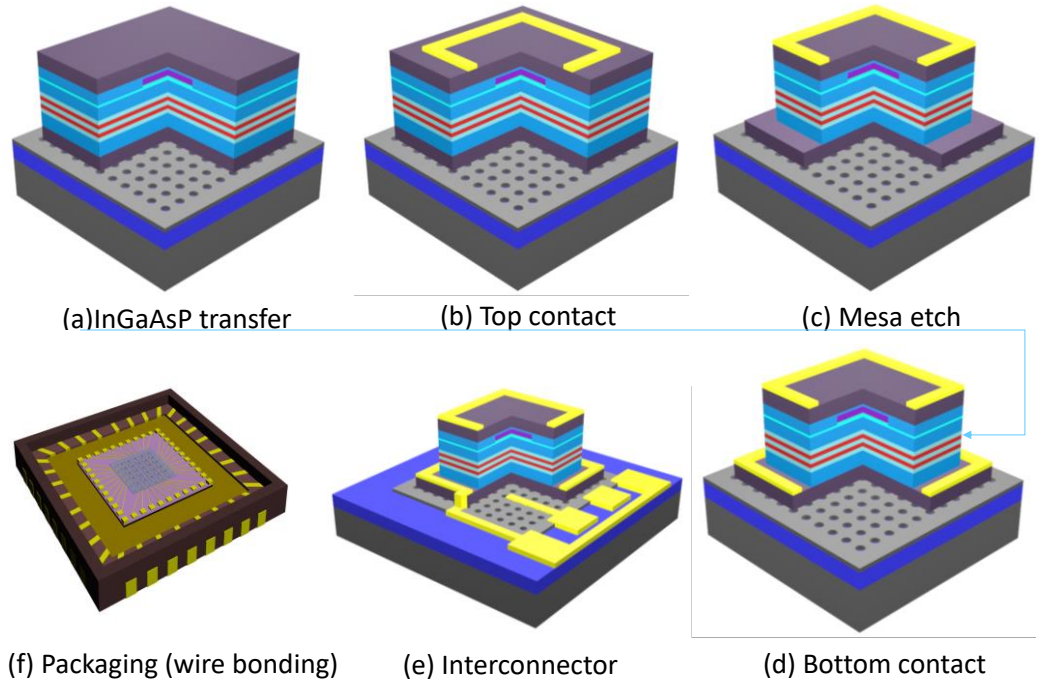

Figure 4-3 Schematic of the steps to fabricate electrically pumped BTJ PCSEL.

The Figure 4-3(a) shows schematic of a InGaAsP MQW membrane with embedded BTJ structure transferred and printing on Si-PC. Second, the top contact step requires the standard photolithography, O_2 plasma treatment, metal deposition and a liftoff process. For this contact mask, a negative resist (NR-9 3000PY) is transferred onto the InGaAsP MQW membrane to create a resist undercut which is easy for liftoff process.

To remove residue of unwanted resist after developing, oxygen plasma processing is efficient method of surface cleaning.

The devices are then deposited alloy metal of Ni/Ge/Au/Ti/Au (10/20/30/10/200 nm) using AJA electron beam evaporation as shown in Figure 4-3(b). Third, the photolithography using positive resist (AZ-1813) for mesa definition and wet etching are needed. After mesa pattern is perfectly aligned, transferred on the top contacts, and baked to harden the photoresist at 130°C for 60 sec, wet etching is employed to etch through the top cladding layers, QW layers, and bottom cladding layer until reaching bottom *n*-InGaAs contact layer. The p-mesa is formed using selective chemical wet etching solutions consisting of $HF:H_2O_2:H_2O$ (1:1:30) to etch InGaAs at etching rate 2nm/sec, InGaAsP at etching rate 3.5nm/sec, and HCl : H_3PO_4 (1:4) to etch InP at etching rate 5.5nm/sec under stirring hotplate at 50 rpm. This step is very crucial since resist has to be strong enough to protect devices during multiple times of wet etching as shown in Figure 4-3(c). Next, this step is similar to the first one with metal sequence of Ni/Ge/Au/Ti/Au (10/20/30/10/200 nm) on n-InGaAs using AJA electron beam. Then liftoff and cleaning sample by using AZ-300T stripper at 80ºC for 10 to 30 minutes and acetone/isopropyl respectively as shown in Figure 4-3(d). Rapid thermal annealing (RTA) in N_2 ambient is required to make the good ohmic contacts. It is worth to note that RTA is very critical for our devices. Therefore, in our case we use well calibrated annealing recipe at 200/340/200ºC for 30/120/30 sec following by checking I-V characteristics of devices before and after RTA. Next step is SiO_2 deposition to passivate the devices. The mesas are now covered by thin layer of SiO_2 with thickness of 500 nm. Then photolithography using open-hole mask is transferred pattern to the top surface of devices. Similarly, plasma processing can be employed to remove unclean patterning area after developing. In the etching scheme, the combination of selective wet etching

and RIE etching are employed to etch away opening area of thin SiO_2 layer. In our case, RIE etching (power=150 watts; pressure=130 mtorr; gas CF_4=25 sccm; etching rate=50 nm/min) has been using to etch about 90% of total thickness of SiO_2 and other 10% of the remaining SiO_2 will be etched by selective wet etching solution of HF (49%):H2O=1:10 with etching rate of SiO_2 about 1 nm/sec. In the following, the I-V characteristics were applied to make sure the open hole etched through the top and bottom contact metal.

Finally, the last step is to generate the interconnector metal for wire bonding. The standard NR9-3000PY resist was used and the pattern transferred onto both p-ring and n-ring contacts. Then O_2 plasma is applied to remove the residue of resist after developing. Then contact metallization with layer sequence of Ti/Au (20/200 nm) is evaporated at slow deposition rate. After finishing metallization, left sample inside the vacuum chamber for an hour before taking it out for better bonding adhesion. Then sample is immerged in AZ-300T stripper at 80ºC for 30 minutes for liftoff process before it is gently cleaned with acetone/ isopropyl as shown in Figure 4-3(e). The sample was mounted on a chip carrier using silver paint, and gold wires was bonded from the interconnector metal to the edge of chip carrier using Wire-Bonder-Kulicke-4524 as shown in Figure 4-3(f).

Figure 4-4 shows the top view micrograph images of 4 x 4 electrically pumped BTJ-PCSEL on Si substrate. The two mesas were peeling off during the process, the bonding energy between the Si-PC and InGaAsP could be improved by further annealing process. Please note the 4 x 4 square mesa array with various sizes are defined by optical lithography alignment and etching process, with alignment accuracy around 1–2 μm. Also, in our mask layout, we design the device dimension to be 77 μm, 87 μm, 122

μm, and 152 μm to have sufficient coupling and QW efficiency, with the corresponding aperture size of 5 μm, 15 μm, 50 μm, and 80 μm, respectively.

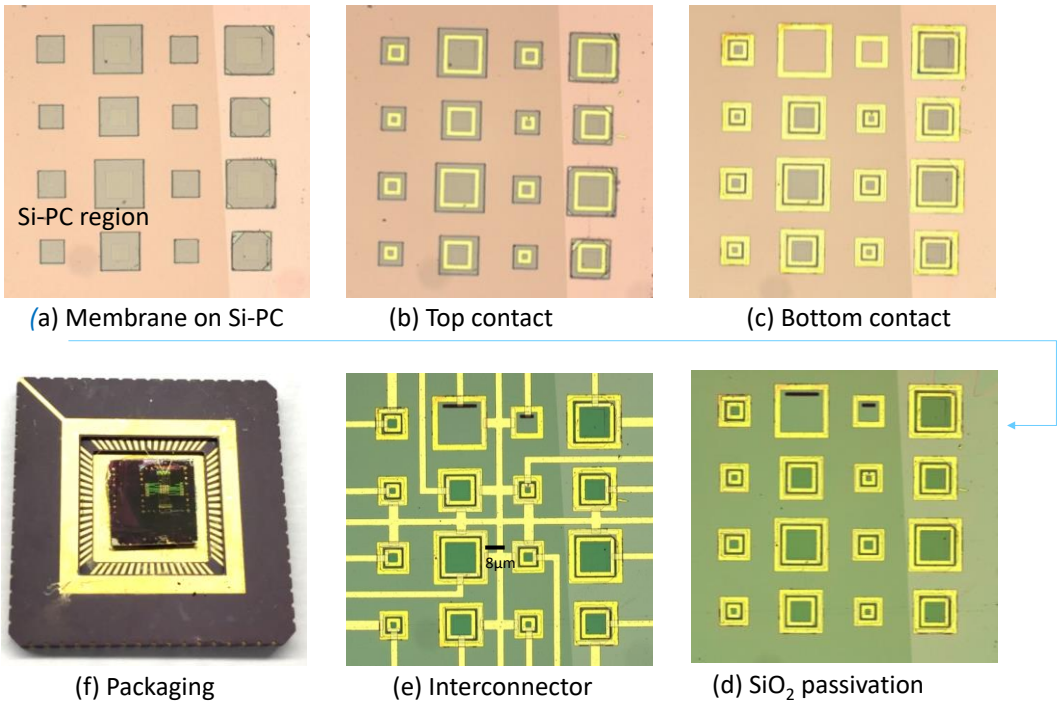

(a) Membrane on Si-PC (b) Top contact (c) Bottom contact

(f) Packaging (e) Interconnector (d) SiO_2 passivation

Figure 4-4 Fabricated 4 x 4 electrically pumped BTJ PCSELs on Si substrate. (a) InGaAsP membrane transferred printing on Si-PC cavity. (b) After top metal contact. (c) After bottom metal contact. (d) After SiO_2 passivation. (e) Interconnector. (f) Packaging and wire bonding.

4.2.2 Current Voltage Characteristics

The measured current voltage (I-V) characteristics of the various sizes BTJ electrically pumped PCSELs were analyzed and compared, as shown in Figure 4-5(a). For the different BTJ size devices, it is observed that as the BTJ size increases, the forward biased current increases. The forward bias region begins operation when the terminal voltage is positive. In this region, the IV relationship can be characterized by:

$$I = I_o(e^{\frac{qV}{nkT}} - 1) \quad (7)$$

Please note *I* is the current through the diode, V is the voltage across the diode, I_o is the dark saturation current, *n* is the ideality factor, and T is the temperature in kelvin. q and k are both constants. I_o is a constant value that is given to a specific diode at a given temperature. The value of linear scale reference current, I_o, is directly proportional to the cross-sectional area of the given junction diode. Here the cross-sectional area of the junction diode is defined by the BTJ dimension. The Individual devices were characterized and plotted as semilog scale shown in Figure 4-5(b), with color in blue, green, black, and red represented for 5 μm, 15 μm, 50 μm, and 80 μm BTJ size, respectively.

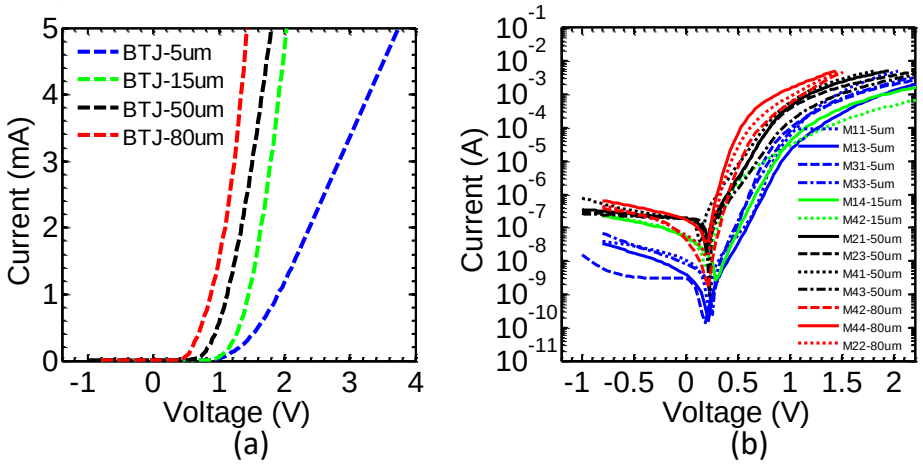

Figure 4-5 (a) I-V curves of devices with different BTJ dimension in linear scale. (b) Log scale.

To better understand the diode properties, the ideality factor in the forward bias and dark current in the reverse bias are theoretical and numerical analysis. From equation (7), the -1 term can be ignored when V > 50 - 100 mV and so the above equation reduces to [59]:

$$I = I_0 exp\left(\frac{qV}{nKT}\right) \tag{8}$$

taking the log of both sides of the equation gives:

$$Ln(I) = Ln(I_0) + \left(\frac{q}{nKT}\right)V \tag{9}$$

When plotting the natural log of the current against the voltage, the slope gives q/nkT and the intercept gives ln(I_0). In real cells the ideality factor depends on the voltage across the cell. The ideality factor can either be plotted as a function of voltage or it can be given as a single value. Here we extract the ideality factor at forward bias at 1V and plot versus the BTJ size, as shown in Figure 4-6(a). We can observe that the value of ideality factor was barely changing as the BTJ size increase. The ideality factor of a diode is a measure of how closely the diode follows the ideal diode equation. The ideal diode equation

assumes that all the recombination occurs via band to band or recombination via traps in the bulk areas from the device In practice, the value of ideality factor should be in the range of 1 - 2 in order to achieve the ideal recombination scheme. The average ideality factor for the BTJ device is around 1.8 - 2 from our experimental results, which indicates the design of our BTJ MQW epitaxy process is good.

The dark current is the relatively small electric current that flows through cross-sectional area of the junction diode even when no photons are entering the device. It is referred to as reverse bias leakage current in non-optical devices and is present in all diodes. Physically, dark current is due to the random generation of electrons and holes within the depletion region of the device. Figure 4-6(b) shows the measured dark current with respect to different BTJ size at V= -0.8 V. The trace of the dark current values exhibits slight quadratic than linear characteristics. This trend indicates the dominant current component is from bulk surface (quadratic) leakage current rather than sidewall leakage (linear). This encouraged result points out that the BTJ structure indeed secures the current injection through the center of MQW to avoid the non-ideal leak current from the sidewall [60].

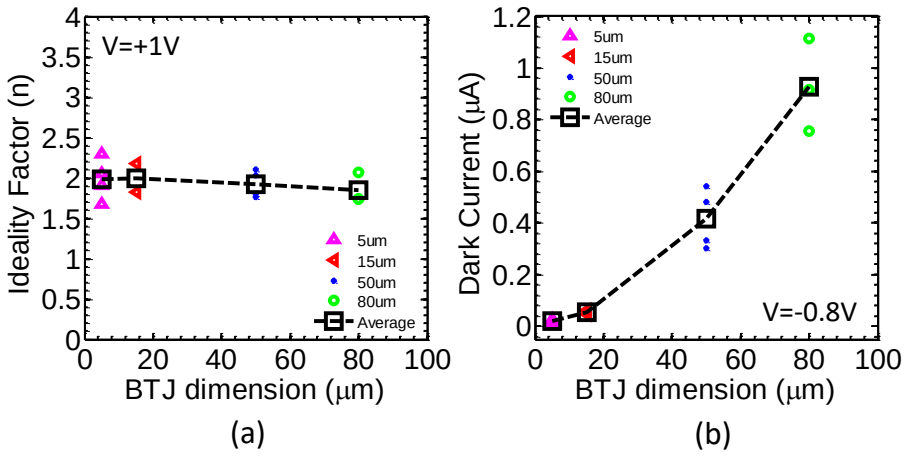

Figure 4-6 (a) Ideality factory - BTJ dimension relationship of the applied bias at 1V. (b) Dark current with respect to different BTJ dimension at -0.8V biased current.

4.3 Device Characteristics

The design and fabrication of the BTJ-PCSEL operating at room temperature (RT) were discussed in previous sections. In order to realize the electrically pumped operation, the BTJ was utilized and inserted into InGaAsP MQW structure to achieve the efficiency current injection. Before introducing the electrically lasing characteristics, the laser peak location, threshold, and linewidth were first measured using optical pumped operation. The Figure 3-1 shows the measurement setup outline. Figure 4-7(a) shows the lasing spectra at different pump power under room temperature operation. The peak location is observed at 1,504 nm with a pumped threshold of ~3 mW. A lasing spectrum above the threshold with a linewidth of 0.6 nm was measured in Figure 4-7(b). The results indicate the laser cavity agrees with the theoretical design and the QW is working functional.

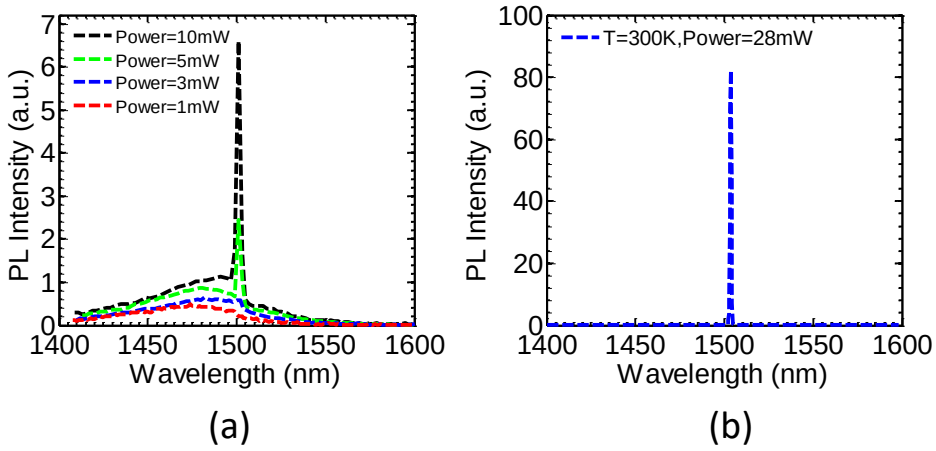

Figure 4-7 (a) Optically pumped lasing spectra from our BTJ PCSEL as a function of optical pumping power at room temperature. (b) Emission spectrum of the laser above threshold.

The electrically pumped lasing characteristics were tested in the continuous-wave (c.w.) mode via wire bonding, without any heat sinking. The laser output from

device is sent into the monochrometer and detected with a thermoelectric-cooled InGaAs photodetector. A chopper and lock-in amplifier are used for the spectral acquisition of lasing output. An infrared (IR) camera is mounted at the other output port of the monochrometer to acquire the far field image. A polarizer is placed in front of the entrance of the monochrometer to investigate the polarization properties of the emission beams.

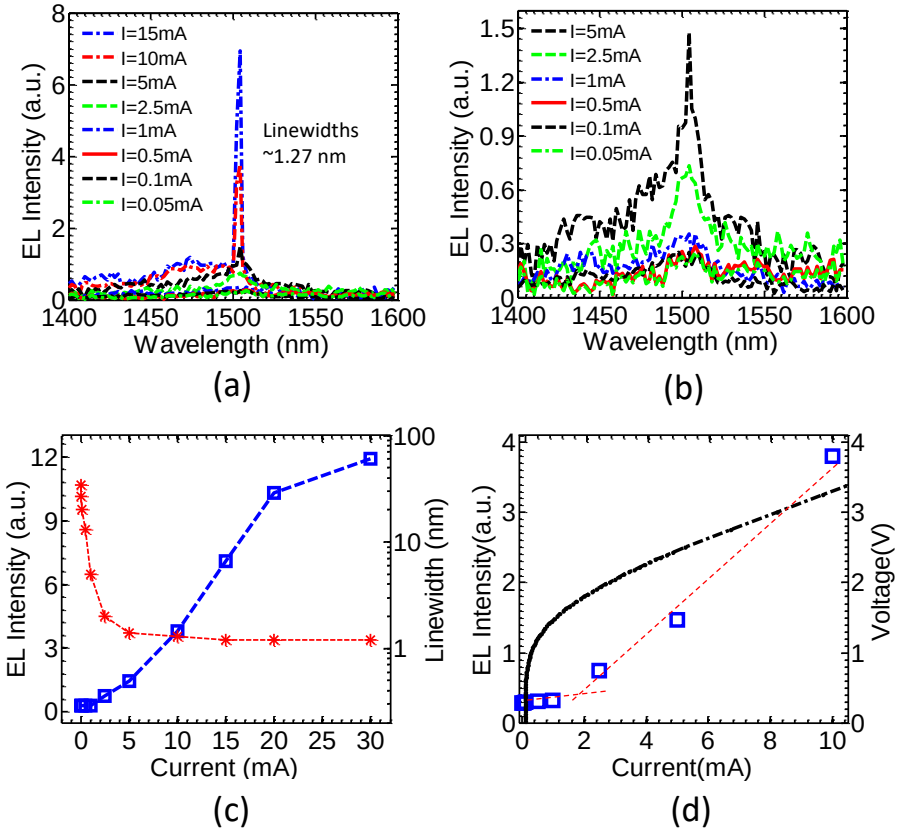

Figure 4-8 (a) Electrically pumped lasing spectra from a 50 x 50 μm^2 BTJ PCSEL device at different bias current level. (b) Zoom-in view of bias current at 0.05 mA to 5 mA. (c) L-I characteristics and linewidths versus the bias current. (d) C.W. L-I-V characteristics of the BTJ PCSEL. The ridge of the BTJ dimension is 50 μm in both width and length.

Figure 4-8(b) shows the laser spectrum at different biased current in to reveal emission centered at 1,504 nm and Full Width Half Maximum (FWHM) value around 1.27

nm. Figure 4-8(b) shows the same laser spectrum but zoomed-in at 0.05 mA to 5 mA biased current level, the measured spectral linewidths are reduced from broadband spectrum to narrowing above 0.1 mA. The measured light-current (L-I) curves was shown in Figure 4-8(c) along with the linewidths reduced from ~35 nm (below threshold) to 1.27 nm (above threshold). A stable single mode performance with a threshold current of about 2 mA has been observed for this laser. The zoomed-in view light-current-voltage (L-I-V) curves at the short bias current range from 0.05 to 10 mA is shown in Figure 4-8(d). At room temperature, cw threshold current density (J_{th}) was calculated to be around 31.25 A/cm^2 for a electrically pumped PCSEL with a 50 x 50 μm^2 dimension, which is relatively lower than reported references.

Shown in Figure 4-9(a) is the measured lasing spectrum above threshold. A dominant single mode peak was observed at around 1,504.3 nm with a narrow linewidth of 1.27 nm, which is essentially limited by the measurement set-up. The side mode suppression ratio (SMSR) reaches ~10.1 dB for the bias current I = 10 mA. Additionally the lasing output shows one dominant polarization, as shown in Figure 4-9(b).

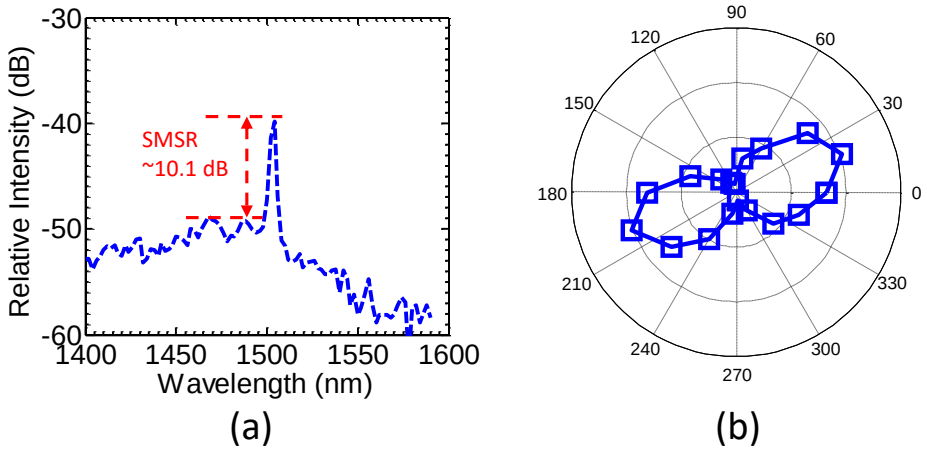

Figure 4-9 (a) A measured output spectrum at an injection current of 10 mA, which shows a side mode suppression ratio of about 10.1dB. (b) Measured polarization properties above threshold at λ = 1,504 nm.

4.4 Discussion and Analysis

Basically, a BTJ uses reversed bias to provide hole injection by feeding the electron current. Several advantages for efficiency current injection have been observed by introducing BTJ in PCSEL. To explain why such a electrically pumped operation can be obtained, we discuss here the points that differ from those of previous works [39-41]. First, the BTJ located on top of the active region allows selective tunneling current injection and the areas outside the active region without the tunnel junction automatically serves as the current blocking function. Second, the regrown *n* doping InP cladding layers with relatively small refractive index form the real index-guiding structure and reduce internal loss. Last, this BTJ-PCSEL requires only one step regrowth, and the BTJ located on top of the active region serves as window areas and assist current flowing from *p*-type InP cladding layers to *n*-type InP cladding layers and then to top *n*-contact layers. That is, both contacts of the lasers are *n* type, except that the top contact is positively charged and the bottom contact is negatively charged.

It is interesting to understand the output beam profile from the BTJ-PCSEL. Additional studies are being conducted to conclusively confirm this. The 4 x 4 arrays of electrically pumped BTJ PCSEL were shown in Figure 4-10(a). The lasing characteristics of the device M22 has been discussed in previous section, here we continue use this device to analysis the beam profile. The overview image of a 4 x 4 BTJ PCSELs were captured using an IR camera as shown in Figure 4-10(b). The near-field IR camera picture shown as Figure 4-10(c) indicates a beam profile with nearly square symmetry. Beam profile has been observed for a round square diameter of 50 μm. This provides further evidence for strong optical coherence over extremely large areas using BTJ. We attribute to the current injection from the top contact was confined within the small

aperture of the *p*++/*n*++ high doping BTJ region. One can see that by using the BTJ for current confinement, the laser shows greatly improving performance.

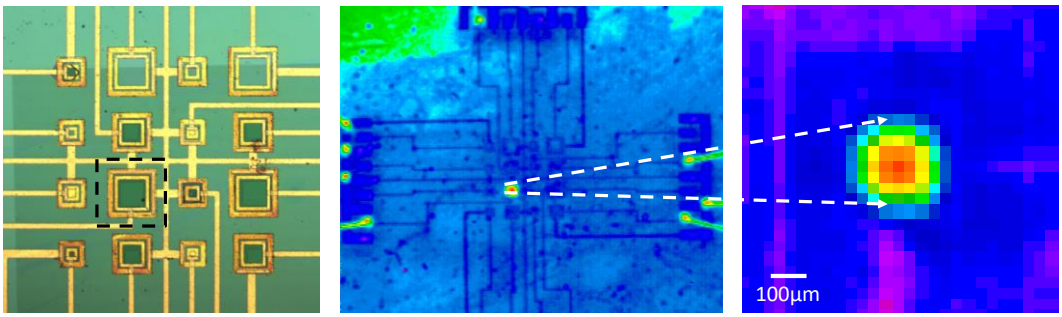

Figure 4-10 (a) Micrographs of a 4x4 array of electrically pumped BTJ PCSEL. (b) Overall view of device image captured from IR camera. (c) Zoom-in view of the 2D beam profile from device M22 with 50 x 50 μm^2 BTJ dimension.

In addition, the experiment results are also correlated to theoretical and numerical analysis. Here we optimized and tuned the Fano/guided resonance modes of the laser cavity according to the simulation. All the spectral simulations are employed by using the Fourier Modal Method with Stanford Stratified Structure Solver (S_4) software package. In our calculations, only the vertical radiation loss is considered as the in-plane loss, and the internal loss is negligible [41]. Figure 4-11(a) shows the Fano/guided resonance modes of the BTJ PCSEL cavities, which can correspond to the dips in the transmission spectra.

The cross-section views of E-field intensity of modes B located at around 1,504 nm are shown in Figure 4-11(d). One can see the field is strongly confined inside the thin cavity due to high index contrast below and above the laser cavity. The confinement factor for the TE band modes is calculated according to fundamental equation discussed in chapter 2. The confinement factors of the mode B located at 1504 nm is calculated to be around 9% for BTJ PCSEL. The relatively high field confinement in Si-PC region indicates the BTJ structure not only offers an efficiency current injection capability, but

also keeps the original functionality of mode confinement. Consequently, lasing spectrum under electrically pumped operation was achieved in BTJ PCSEL in experiments, including the lower threshold and narrower linewidth, which agrees well with theoretical design and analysis.

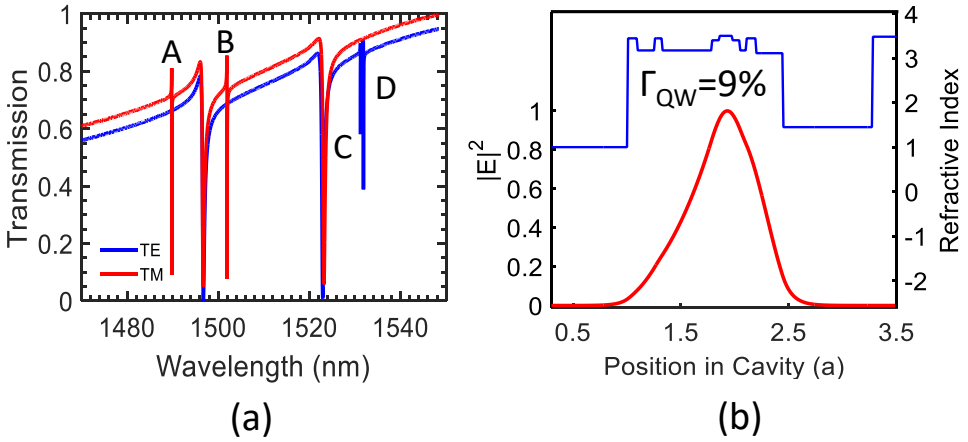

Figure 4-11 (a) Fano/guided resonance modes of the BTJ PCSEL cavities. (b) Field distribution of mode B from BTJ PCSEL at room temperature operation.

Chapter 5

Concluding Remark and Future Research

In this thesis, various kinds of silicon photonic crystal (Si-PC) cavities have been experimentally demonstrated. The bandedge effect in PC structures, where the group velocity is close to zero, has advantages in achieving high performance semiconductor surface emitting lasers, including low lasing threshold, single longitudinal and transverse mode over a large lasing area, narrow linewidth, high power output, small beam divergence angle, polarization control, and output beam pattern control. Different designs of Si-PC cavities were fabricated for different operation temperature. By employing membrane transfer and printing technique, hybrid photonic crystal surface emitting lasers (PCSELs) are demonstrated with optical pumping. With the careful cavity design and the control of the transfer process, single mode lasing was achieved with narrowing linewidth ~7 Å and side mode suppression ratio of 28 dB for devices operating at 25K-180K. Moreover, In order to achieve room-temperature operation device in such a cavity, it is highly desirable to design a cavity with the following characteristics: (1) Two-dimensional (2D) square lattices Si-PC structure is designed to have a lattice constant of 480 nm, based on the second-order Bragg diffraction condition; (2) the cavity mode distribution should match with MQW emission peak, with the hole radius and thickness of Si-PC slab designed to be 72 nm (r = 0.15a) and 190 nm, respectively; (3) the separation distance between the InGaAsP multi-quantum well (MQW) layer and Si-PC slab is reduced to enhance the in-plane coupling efficiency. Single mode lasing under room temperature (RT) operation was observed at 1,542 nm, with excellent linewidth ~5.4 Å and side mode suppression ration (SMSR) of 32.4 dB, for the laser built on silicon on insulator (SOI) substrate operating at room temperature. Another important cavity design of the PCSEL directly built on bulk Si substrate was also reported in this work. The excellent heat

dissipation from the active region and minimized temperature rise of the lasing cavity were also demonstrated experimentally, and agree well with the thermal simulation.

The lateral confinement effect associated with device size in Si based PCSEL has yet to be investigated in detail. Typically, the PCSEL devices we demonstrated so far have relatively large lateral dimension, typically around 150 -300 μm. Such a large in-plane size can be regarded as an infinite structure, so the lateral loss will be very small and can be ignored. On the contrary, when the device size becomes smaller, the lateral loss will have significant impact on the mode properties such as quality factor (Q), confinement factor (Γ_{QW}), SMSR, and gain threshold (g_{th}). Therefore, the laser characteristics are not keeping better with the dimension shrinks due to loss of lateral confinement, resulting in a bottleneck in the reach for ultra-compact volume of optical circuit. To address this issue, various devices with different cavity dimension were fabricated to investigate the lasing characteristics dependent on pumping spot size and device dimension. The results indicate that the when the pump spot size or device dimension is relatively small, the cavity is excited at a state of weak lateral confinement with low coupling efficiency. Due to the deficiency of coupling, the laser threshold is much higher compared to the sufficient coupling strength. Conversely, when the pump spot or device dimension is increased to overcome another limit, the device will be excited at a state of strong lateral confinement with over coupling efficiency. Hence, the laser threshold density cannot be further decreased and reaches a saturation value. We also found that the adjacent grating and bottom metal reflector are able to mitigate the in-plane loss at the device boundary. All the results here give us the guidance and confidence to achieve smaller PCSEL devices with better performances.

Finally, we report the design and demonstration of a room temperature electrically pumped PCSEL on Si substrate by employing buried tunneling junction (BTJ)

structure as a current spreading control. The current injection from the top contact was confined and passes through the small aperture of the *p*++/*n*++ high doping BTJ region. A dominant single mode peak was observed at around 1504.3 nm with a narrow linewidth of 1.27 nm, which is essentially limited by the measurement set-up. The SMSR reaches ~10.1 dB above the threshold.

All experimental results were correlated to the numerical analysis, and agree well with the theoretical expectations. These results indicate that the combination of the transfer printing process and the photonic crystal designed in bandedge effect offers a simple and flexible method to realize single mode high power lasers for large-scale silicon-based photonic integration. Further optimization of the cavity design and improvement of the fabrication quality can lead to the realization of higher performance, high power electrically pumped lasers with potential 2D multi-wavelength arrays for on-chip multi-layer wavelength-division multiplexing (WDM) systems with the desired spectral, spatial, and energy-efficiency.

Appendix A

List of Publications

Journal Publications

1. **S.-C. Liu**, D. Zhao, X. Ge, H. Yang, Z. Ma, and W. Zhou, “Electrically pumped buried tunneling junction photonic crystal surface emitting laser” In preparation.
2. **S.-C. Liu**, D. Zhao, X. Ge, H. Yang, Z. Ma, and W. Zhou, “Lateral Size Scaling of Photonic Crystal Surface Emitting Lasers on Si Substrate” In preparation.
3. H. Wang, **S.-C. Liu**, B. Balachandran, J. Moon, R. Haroldson, Z. Li, A. Ishteev, Q. Gu, W. Zhou, A. Zakhidov and W. Hu, “Nanoimprinted Perovskite Metasurface for Enhanced Photoluminescence”, Optics Express, vol. 25 pp1162-1171 (2017).
4. **S.-C. Liu**, D. Zhao, Y. Liu, H. Yang, Y. Sun, Z. Ma, C. Reuterskiöld-Hedlund, M. Hammar, and W. Zhou, “Photonic crystal bandedge membrane lasers on silicon”, Applied Optics, vol. 56 pp 67-73 (2017).
5. D. Lee, J. Lee, K. Song, F. Xue, S-Y. Choi, Y. Ma, J. Podkaminer, D. Liu, **S.-C. Liu**, B. Chung, W. Fan, S. J. Cho, W. Zhou, J. Lee, L.-Q. Chen, S. H. Oh, Z. Ma, C.-B. Eom, “Sharpened VO2 phase transition via controlled release of epitaxial strain”, Nano Letter, vol17, pp 1514-5619 (2017)
6. M. Kim, J.-H. Seo, D. Zhao, **S.-C. Liu**, K. Kim, K. Lim, W. Zhou, E. Waks and Z. Ma, “Transferrable single crystalline 4H-SiC nanomembranes”, J. Mater. Chem. C, vol. 5, pp.264-268 (2017)
7. M. Kim, **S.-C. Liu**, T. J. Kim, J. Lee, J.-H. Seo, W. Zhou, and Z. Ma, “Light absorption enhancement in Ge nanomembrane and its optoelectronic application”, Optics Express, vol. 24, pp.16984-16903 (2016).
8. T.-H. Chang, W. Fan, **S.-C. Liu**, L. Menon, J. Yang, W. Zhou and Z. Ma, “Selective release of InP heterostructures from InP substrates”, Journal of Vacuum Science and Technology B, vol. 34, 041229 (2016).
9. M. Cho , J.-H. Seo , D. Zhao , J. Lee , K. Xiong , X. Yin , Y. Liu , **S.-C. Liu** , M. Kim , T. J Kim , X. Wang , W. Zhou, Z. Ma, "Amorphous Si/SiO2 distributed Bragg reflectors with transfer printed single-crystalline Si nanomembranes", Journal of Vacuum Science and Technology B, 34, 040601 (2016).
10. D. Zhao*, **S.-C. Liu***, H. Yang, Z. Ma, C. R. Hedlund, M. Hammar and W. Zhou, “Printed Large-Area Single-Mode Photonic Crystal Bandedge Surface-Emitting Lasers on Silicon”, Scientific Report, vol. 6, pp18860 (2016). *equal contribution.
11. H. Yang, D. Zhao, **S.-C. Liu**, Y. Liu, J.–H. Seo, Z. Ma and W. Zhou, “Transfer Printed Nanomembranes for Heterogeneously Integrated Membrane Photonics”, Photonics, vol. 2, pp.1081-1100 (2015).
12. M. Kim, W. Fan, J.-H. Seo, N. Cho, **S.-C. Liu**, D. Geng, S. Gong, W. Zhou, X. Wang and Z. Ma, "Polycrystalline GeSn thin film on Si formed by alloy evaporation," Applied Physics Express, 8 061301 (2015).
13. **S.-C. Liu**, D. Zhao, J.-H. Seo, Y. Liu, Z. Ma and W. Zhou, “Athermal Photonic Crystal Membrane Reflectors on Diamond”, IEEE Photonics Technology Letters, vol. 27, pp.1072 (2015).

Conference

1. H. Wang, B. Balasubramaniam, R. Haroldson, A. Gharajeh, D. Zhao, Z. Li, J. Moon, **S.-C. Liu**, J. Y. Chan, W. Zhou, S. Makarov, Q. Gu, A. Zakhidov, W. Hu, "Nanoimprinted Perovskite for Optoelectronics", IEEE NANO, Pittsburg, PA, Jul. 25-28 (2017).
2. A. Gharajeh, H. Wang, Z. Li, J. Moon, R. Haroldson, B. Balasubramaniam, D. Zhao, S.-C. Liu, W. Zhou, S. Makarov, A. Zakhidov, W. Hu, Q. Gu, "Amplified Spontaneous Emission in Nanoimprinted Perovskite Nanograting Metasurface", IEEE NANO, Pittsburg, PA, Jul. 25-28 (2017).
3. **S.-C. Liu**, D. Zhao, Y. Liu, H. Yang, C. Reuterskiöld-Hedlund, M. Hammar, Z. Ma, W. Zhou, "Photonic crystal surface-emitting lasers on silicon substrates", Photonics Society Summer Topical Meeting Series (SUM), San Juan, PR, Jul. 10-12 (2017).
4. M. Kim, S. Yi, J. D. Kim, **S.-C. Liu**, W. Zhou, Z.Yu, X. Li, "Munho Kim, Soongyu Yi, Jeong Dong Kim, Shih-Chia Liu, Weidong Zhou, Zongfu Yu, Xiuling Li", Device Research Conference (DRC), Notre Dame, IN, Jun. 25-28 (2017).
5. **S.-C. Liu**, D. Zhao, H. Yang, C. Reuterskiöld-Hedlund, M. Hammar, Z. Ma, W. Zhou, "Photonic Crystal Surface-Emitting Lasers on Bulk Silicon Substrate", *CLEO*, San Jose, CA, May. 14-19 (2017).
6. **S.-C. Liu**, D. Zhao, H. Yang, C. Reuterskiöld-Hedlund, M. Hammar, S. Fan, Z. Ma, W. Zhou, "Lateral Size Scaling of Photonic Crystal Surface-Emitting Lasers on Si", *CLEO*, San Jose, CA, May. 14-19 (2017).
7. W. Zhou, **S.-C. Liu**, D. Zhao, H. Yang, M. Hammar, Z. Ma, "Seminconductor photonic crystal membrane lasers for 3D integration on", SPIE Photonics West, San Francisco, CA, Feb 2-7 (2017).
8. W. Zhou, **S.-C. Liu**, D. Zhao, H. Yang, Z. Ma and M. Hammar, "Hybrid Photonic Crystal Membrane Lasers on Silicon", Proceedings of Materials Research Society (MRS), Boston, MA, Nov. 27-Dec. 2 (2016)
9. W. Zhou, **S.-C. Liu**, D. Zhao, H. Yang, Z. Ma, M. Hammar, "Printed Photonic Crystal Membrane Lasers on Silicon", Asia Communications and Photonics Conference, Wuhan, China, Nov. 2-5 (2016).
10. D. Zhao, **S.-C. Liu**, H. Yang, Z. Ma, W. Zhou, "Deyin Zhao, Shih-Chia Liu, Hongjun Yang, Zhenqiang Ma, Weidong Zhou", PIERS, Shanghai, China, Aug. 8-11 (2016)
11. **S.-C. Liu**, D. Zhao, H. Yang, Z. Ma, C. R. Hedlund, M. Hammar and W. Zhou, "Room Temperature Photonic Crystal Bandedge Membrane Lasers on SOI Substrates", *CLEO*, San Jose, CA, Jun. 5-10 (2016).
12. H. Yang, D. Zhao, **S.-C. Liu**, Y. Liu, J.-H. Seo, M. Hodek, Z. Ma, J. Albrecht, B. Moody, W. Zhou, "High-Reflectivity DUV Mirrors Prepared by Direct Sputtering", *CLEO*, San Jose, CA, Jun. 5-10 (2016).
13. D. Zhao, **S.-C. Liu**, H. Yang, Z. Ma, C. R. Hedlund, M. Hammar and W. Zhou, "Design and characterization of photonic crystal bandedge surface-emitting lasers on silicon", IEEE Photonics Conference (IPC), Reston, VA, Oct.4-8 (2015).
14. **S.-C. Liu**, D. Zhao, H. Yang, Z. Ma, C. R. Hedlund, M. Hammar and W. Zhou, "Printed Photonic Crystal Bandedge Surface-emitting Lasers on Silicon", *CLEO*, San Jose, CA, May. 10-15 (2015).

15. **S.-C. Liu**, D. Zhao, J.-H. Seo, Y. Liu, Z. Ma and W. Zhou, “Thermally engineered photonic crystal membrane reflectors based on transferred nanomembranes on diamond”, IEEE Photonics Conference (IPC), San Diego, CA, Oct. 12-16 (2014).
16. D. Zhao, A. S. Chadha, **S.-C. Liu**, H. Yang, Z. Ma and W. Zhou, “Surface-normal photonic Crystal Membrane Reflector with Integrated In-Plane Coupler for Silicon Photonics Integration”, IEEE Photonics Conference (IPC), San Diego, CA, Oct. 12-16 (2014).

References

[1] T. Barwicz, H. Byun, F. Gan, C. W. Holzwarth, M. A. Popovic, P. T. Rakich, et al., "Silicon photonics for compact, energy-efficient interconnects [Invited]," Journal of Optical Networking, vol. 6, pp. 63-73, 2007/01/01 2007.

[2] S. Papaioannou, D. Fitsios, G. Dabos, K. Vyrsokinos, G. Giannoulis, A. Prinzen, et al., "On-Chip Dual-Stream DWDM Eight-Channel-Capable SOI-Based MUX s/DEMUX s With 40-GH z Channel Bandwidth," IEEE Photonics Journal, vol. 7, pp. 1-10, 2015.

[3] Z. Cheng and H. K. Tsang, "Experimental demonstration of polarization-insensitive air-cladding grating couplers for silicon-on-insulator waveguides," Optics Letters, vol. 39, pp. 2206-2209, 2014/04/01 2014.

[4] G. T. Reed, G. Mashanovich, F. Y. Gardes, and D. J. Thomson, "Silicon optical modulators," Nature Photonics, vol. 4, p. 518, 07/30/online 2010.

[5] L. Alloatti, D. Korn, R. Palmer, D. Hillerkuss, J. Li, A. Barklund, et al., "42.7 Gbit/s electro-optic modulator in silicon technology," Optics Express, vol. 19, pp. 11841-11851, 2011/06/06 2011.

[6] L. Vivien, J. Osmond, J.-M. Fédéli, D. Marris-Morini, P. Crozat, J.-F. Damlencourt, et al., "42 GHz p.i.n Germanium photodetector integrated in a silicon-on-insulator waveguide," Optics Express, vol. 17, pp. 6252-6257, 2009/04/13 2009.

[7] T. Y. Liow, K. W. Ang, Q. Fang, J. F. Song, Y. Z. Xiong, M. B. Yu, et al., "Silicon Modulators and Germanium Photodetectors on SOI: Monolithic Integration, Compatibility, and Performance Optimization," IEEE Journal of Selected Topics in Quantum Electronics, vol. 16, pp. 307-315, 2010.

[8] B. Souhan, R. R. Grote, J. B. Driscoll, M. Lu, A. Stein, H. Bakhru, et al., "Metal-semiconductor-metal ion-implanted Si waveguide photodetectors for C-band operation," Optics Express, vol. 22, pp. 9150-9158, 2014/04/21 2014.

[9] R. Chen, T.-T. D. Tran, K. W. Ng, W. S. Ko, L. C. Chuang, F. G. Sedgwick, et al., "Nanolasers grown on silicon," Nature Photonics, vol. 5, p. 170, 02/06/online 2011.

[10] Z. Mi, P. Bhattacharya, J. Yang, and K. P. Pipe, Room-temperature self-organised In0.5Ga0.5As quantum dot laser on silicon vol. 41, 2005.

[11] G. Balakrishnan, A. Jallipalli, P. Rotella, S. Huang, A. Khoshakhlagh, A. Amtout, et al., "Room-Temperature Optically Pumped (Al)GaSb Vertical-Cavity Surface-Emitting Laser Monolithically Grown on an Si(1 0 0) Substrate," IEEE Journal of Selected Topics in Quantum Electronics, vol. 12, pp. 1636-1641, 2006.

[12] A. W. Fang, P. Hyundai, R. Jones, O. Cohen, M. J. Paniccia, and J. E. Bowers, "A continuous-wave hybrid AlGaInAs-silicon evanescent laser," IEEE Photonics Technology Letters, vol. 18, pp. 1143-1145, 2006.

[13] G. Roelkens, D. V. Thourhout, R. Baets, R. Nötzel, and M. Smit, "Laser emission and photodetection in an InP/InGaAsP layer integrated on and coupled to a Silicon-on-Insulator waveguide circuit," Optics Express, vol. 14, pp. 8154-8159, 2006/09/04 2006.

[14] D. Andrijasevic, M. Austerer, A. M. Andrews, P. Klang, W. Schrenk, and G. Strasser, "Hybrid integration of GaAs quantum cascade lasers with Si substrates by thermocompression bonding," Applied Physics Letters, vol. 92, p. 051117, 2008/02/04 2008.

[15] H.-C. Yuan, Z. Ma, M. M. Roberts, D. E. Savage, and M. G. Lagally, "High-speed strained-single-crystal-silicon thin-film transistors on flexible polymers," Journal of Applied Physics, vol. 100, p. 013708, 2006/07/01 2006.
[16] H.-C. Yuan and Z. Ma, "Microwave thin-film transistors using Si nanomembranes on flexible polymer substrate," Applied Physics Letters, vol. 89, p. 212105, 2006/11/20 2006.
[17] M. A. Meitl, Z.-T. Zhu, V. Kumar, K. J. Lee, X. Feng, Y. Y. Huang, et al., "Transfer printing by kinetic control of adhesion to an elastomeric stamp," Nature Materials, vol. 5, p. 33, 12/11/online 2005.
[18] H.-C. Yuan, G. K. Celler, and Z. Ma, "7.8-GHz flexible thin-film transistors on a low-temperature plastic substrate," Journal of Applied Physics, vol. 102, p. 034501, 2007/08/01 2007.
[19] R.-H. Kim, S. Kim, Y. M. Song, H. Jeong, T.-i. Kim, J. Lee, et al., "Flexible Vertical Light Emitting Diodes," Small, vol. 8, pp. 3123-3128, 2012.
[20] R.-H. Kim, M.-H. Bae, D. G. Kim, H. Cheng, B. H. Kim, D.-H. Kim, et al., "Stretchable, Transparent Graphene Interconnects for Arrays of Microscale Inorganic Light Emitting Diodes on Rubber Substrates," Nano Letters, vol. 11, pp. 3881-3886, 2011/09/14 2011.
[21] L. Sun, G. Qin, J.-H. Seo, G. K. Celler, W. Zhou, and Z. Ma, "12-GHz Thin-Film Transistors on Transferrable Silicon Nanomembranes for High-Performance Flexible Electronics," Small, vol. 6, pp. 2553-2557, 2010.
[22] J. Justice, C. Bower, M. Meitl, M. B. Mooney, M. A. Gubbins, and B. Corbett, "Wafer-scale integration of group III–V lasers on silicon using transfer printing of epitaxial layers," Nature Photonics, vol. 6, p. 610, 08/19/online 2012.
[23] S. Noda, "Photonic crystal lasers—ultimate nanolasers and broad-area coherent lasers [Invited]," Journal of the Optical Society of America B, vol. 27, pp. B1-B8, 2010/11/01 2010.
[24] O. Painter, R. K. Lee, A. Scherer, A. Yariv, J. D. Brien, P. D. Dapkus, et al., "Two-Dimensional Photonic Band-Gap Defect Mode Laser," Science, vol. 284, p. 1819, 1999.
[25] J. K. Hwang, H. Y. Ryu, D. S. Song, I. Y. Han, H. K. Park, and Y. H. Lee, "Continuous room-temperature operation of optically-pumped two dimensional photonic crystal lasers at 1.6 /spl mu/m," in Quantum Electronics and Laser Science Conference (QELS 2000). Technical Digest. Postconference Edition. TOPS Vol.40 (IEEE Cat. No.00CH37089), 2000, pp. 304-305.
[26] W. D. Zhou, J. Sabarinathan, B. Kochman, E. Berg, O. Qasaimeh, S. Pang, et al., "Electrically injected single-defect photonic bandgap surface-emitting laser at room temperature," Electronics Letters, vol. 36, pp. 1541-1542, 2000.
[27] H.-G. Park, S.-H. Kim, S.-H. Kwon, Y.-G. Ju, J.-K. Yang, J.-H. Baek, et al., "Electrically Driven Single-Cell Photonic Crystal Laser," Science, vol. 305, p. 1444, 2004.
[28] H. Altug and J. Vučković, "Photonic crystal nanocavity array laser," Optics Express, vol. 13, pp. 8819-8828, 2005/10/31 2005.
[29] M. Imada, S. Noda, A. Chutinan, T. Tokuda, M. Murata, and G. Sasaki, "Coherent two-dimensional lasing action in surface-emitting laser with triangular-lattice photonic crystal structure," Applied Physics Letters, vol. 75, pp. 316-318, 1999/07/19 1999.
[30] M. Imada, A. Chutinan, S. Noda, and M. Mochizuki, "Multidirectionally distributed feedback photonic crystal lasers," Physical Review B, vol. 65, p. 195306, 04/26/ 2002.

[31] G. Vecchi, F. Raineri, I. Sagnes, A. Yacomotti, P. Monnier, T. J. Karle, et al., "Continuous-wave operation of photonic band-edge laser near 1.55 μm on silicon wafer," Optics Express, vol. 15, pp. 7551-7556, 2007/06/11 2007.
[32] K. Hirose, Y. Liang, Y. Kurosaka, A. Watanabe, T. Sugiyama, and S. Noda, "Watt-class high-power, high-beam-quality photonic-crystal lasers," Nature Photonics, vol. 8, p. 406, 04/13/online 2014.
[33] S. Shi, C. Chen, and D. W. Prather, "Plane-wave expansion method for calculating band structure of photonic crystal slabs with perfectly matched layers," Journal of the Optical Society of America A, vol. 21, pp. 1769-1775, 2004/09/01 2004.
[34] R. J. E. Taylor, "Design of photonic crystal surface emitting laser and the realisation of coherently coupled arrays.," Thesis, 2015.
[35] N. Oleg, "Optical transmitters " Lightwave Russian Edition. , vol. 2, 2003.
[36] H. Yang, D. Zhao, S. Chuwongin, J.-H. Seo, W. Yang, Y. Shuai, et al., "Transfer-printed stacked nanomembrane lasers on silicon," Nature Photonics, vol. 6, p. 615, 07/22/online 2012.
[37] S. Chuwongin, "Nanomembrane surface emitting light sources," Thesis, 2012.
[38] V. Liu and S. Fan, "S4 : A free electromagnetic solver for layered periodic structures," Computer Physics Communications, vol. 183, pp. 2233-2244, 2012/10/01/ 2012.
[39] D. Zhao, S. Liu, H. Yang, Z. Ma, C. Reuterskiöld-Hedlund, M. Hammar, et al., "Printed Large-Area Single-Mode Photonic Crystal Bandedge Surface-Emitting Lasers on Silicon," Scientific Reports, vol. 6, p. 18860, 01/04/online 2016.
[40] S.-C. Liu, D. Zhao, H. Yang, C. Reuterskiöld-Hedlund, M. Hammar, Z. Ma, et al., "Photonic Crystal Surface-Emitting Lasers on Bulk Silicon Substrate," in Conference on Lasers and Electro-Optics, San Jose, California, 2017, p. SM4N.6.
[41] S.-C. Liu, D. Zhao, Y. Liu, H. Yang, Y. Sun, Z. Ma, et al., "Photonic crystal bandedge membrane lasers on silicon," Applied Optics, vol. 56, pp. H67-H73, 2017/11/01 2017.
[42] Y. Liang, C. Peng, K. Sakai, S. Iwahashi, and S. Noda, "Three-dimensional coupled-wave analysis for square-lattice photonic crystal surface emitting lasers with transverse-electric polarization: finite-size effects," Optics Express, vol. 20, pp. 15945-15961, 2012/07/02 2012.
[43] X. Liu, S. Klinkhammer, Z. Wang, T. Wienhold, C. Vannahme, P.-J. Jakobs, et al., "Pump spot size dependent lasing threshold in organic semiconductor DFB lasers fabricated via nanograting transfer," Optics Express, vol. 21, pp. 27697-27706, 2013/11/18 2013.
[44] A. E. Miroshnichenko, S. Flach, and Y. S. Kivshar, "Fano resonances in nanoscale structures," Reviews of Modern Physics, vol. 82, pp. 2257-2298, 08/11/ 2010.
[45] A. F. Oskooi, D. Roundy, M. Ibanescu, P. Bermel, J. D. Joannopoulos, and S. G. Johnson, "Meep: A flexible free-software package for electromagnetic simulations by the FDTD method," Computer Physics Communications, vol. 181, pp. 687-702, 2010/03/01/ 2010.
[46] P. Chaisakul, D. Marris-Morini, J. Frigerio, D. Chrastina, M.-S. Rouifed, S. Cecchi, et al., "Integrated germanium optical interconnects on silicon substrates," Nature Photonics, vol. 8, p. 482, 05/11/online 2014.
[47] N. Sherwood-Droz and M. Lipson, "Scalable 3D dense integration of photonics on bulk silicon," Optics Express, vol. 19, pp. 17758-17765, 2011/08/29 2011.

[48] G. Kim, H. Park, J. Joo, K.-S. Jang, M.-J. Kwack, S. Kim, et al., "Single-chip photonic transceiver based on bulk-silicon, as a chip-level photonic I/O platform for optical interconnects," Scientific Reports, vol. 5, p. 11329, 06/10/online 2015.
[49] B. Song, C. Stagarescu, S. Ristic, A. Behfar, and J. Klamkin, "3D integrated hybrid silicon laser," Optics Express, vol. 24, pp. 10435-10444, 2016/05/16 2016.
[50] J. Ferrara, W. Yang, L. Zhu, P. Qiao, and C. J. Chang-Hasnain, "Heterogeneously integrated long-wavelength VCSEL using silicon high contrast grating on an SOI substrate," Optics Express, vol. 23, pp. 2512-2523, 2015/02/09 2015.
[51] T. Flick, K. H. Becks, J. Dopke, P. Mättig, and P. Tepel, "Measurement of the thermal resistance of VCSEL devices," Journal of Instrumentation, vol. 6, p. C01021, 2011.
[52] H. Lindberg, M. Strassner, E. Gerster, J. Bengtsson, and A. Larsson, "Thermal management of optically pumped long-wavelength InP-based semiconductor disk lasers," IEEE Journal of Selected Topics in Quantum Electronics, vol. 11, pp. 1126-1134, 2005.
[53] S. Liu, D. Zhao, J. H. Seo, Y. Liu, Z. Ma, and W. Zhou, "Athermal Photonic Crystal Membrane Reflectors on Diamond," IEEE Photonics Technology Letters, vol. 27, pp. 1072-1075, 2015.
[54] R. Kobayashi, H. Hotta, F. Miyasaka, K. Hara, and K. Kobayashi, "Real index-guided AlGaInP visible laser with high-bandgap energy AlInP current blocking layer grown by HCl-assisted metalorganic vapor phase epitaxy," IEEE Journal of Selected Topics in Quantum Electronics, vol. 1, pp. 723-727, 1995.
[55] M. Ortsiefer, W. Hofmann, J. Rosskopf, and M.-C. Amann, "Long-Wavelength VCSELs with Buried Tunnel Junction," in VCSELs: Fundamentals, Technology and Applications of Vertical-Cavity Surface-Emitting Lasers, R. Michalzik, Ed., ed Berlin, Heidelberg: Springer Berlin Heidelberg, 2013, pp. 321-351.
[56] W. Hofmann, C. Chase, M. Müller, Y. Rao, C. Grasse, G. Böhm, et al., "Long-Wavelength High-Contrast Grating Vertical-Cavity Surface-Emitting Laser," IEEE Photonics Journal, vol. 2, pp. 415-422, 2010.
[57] S. Arafin, A. Bachmann, and M. C. Amann, "Transverse-Mode Characteristics of GaSb-Based VCSELs With Buried-Tunnel Junctions," IEEE Journal of Selected Topics in Quantum Electronics, vol. 17, pp. 1576-1583, 2011.
[58] W. Hofmann, "High-Speed Buried Tunnel Junction Vertical-Cavity Surface-Emitting Lasers," IEEE Photonics Journal, vol. 2, pp. 802-815, 2010.
[59] K. R. McIntosh and C. B. Honsberg, "The Influence of Edge Recombination on a Solar Cell's IV Curve," in 16th European Photovoltaic Solar Energy Conference, ed, 2000.
[60] M.-S. Park, M. Razaei, K. Barnhart, C. L. Tan, and H. Mohseni, "Surface passivation and aging of InGaAs/InP heterojunction phototransistors," Journal of Applied Physics, vol. 121, p. 233105, 2017/06/21 2017.

Biographical Information

Shih-Chia was born in Yunlin, Taiwan. He received his Bachelor degree in 2006 from Taiwan Chung Cheng University, specializing in Physics. In 2008, he obtained his Master's degree in Electro-Optical Engineering from Taiwan Chiao-Tung University. His focus was on quantum dot photodetector and MEMS.

In Fall 2012, Shih-Chia joined Dr. Weidong Zhou's Nanophotonics group at University of Texas at Arlington as a PhD candidate. His research interests include design, fabrication and characterization of hybrid III-V/Si photonic crystal Laser to obtain on-chip silicon based light source in photonics integrated circuit (PIC). He has worked on VCSEL and PCSEL Si based laser, with an emphasis on fabrication of active devices with photonic crystal structure. He has also worked on optics modeling and thermal simulation for laser cavity. He had a talent for 3D sketches of optoelectronics device, modulator, and packaging component using 3D max and solid work.

Shih-Chia's research interests include applied aspects of nanofabrication for 1310-1550 nm hybrid GaAs/InP Si photonics lasers for optics communication. Shih-Chia plans to pursue a career on nanofabrication, development and packaging of novel and unusual Si photonics integrated circuit.